Chemical Science

ROYAL SOCIETY OF CHEMISTRY

REVIEW

View Article Online
View Journal

Check for updates

Cite this: DOI: 10.1039/d5sc08028b

Recent advances in lead halide perovskite single crystals for optoelectronic devices

Lu Zi, *[a] Ximan Fan,[a] Le Liu,[b] Shuna Guan,[a] Hongxian Wei,[a] Jiaqi Chen,[a] Xiaojuan Zhuang*[a] and Wen Xu*[c]

Received 17th October 2025
Accepted 20th January 2026

DOI: 10.1039/d5sc08028b

rsc.li/chemical-science

Over the past decade, perovskite materials have driven significant innovations in optoelectronics due to their exceptional photoelectric performance, drawing substantial global research attention. Specifically, the certified power conversion efficiency (PCE) of single-junction perovskite solar cells has reached 27.37%, the X-ray light yield of perovskite scintillators has attained 1 20 000 photons per MeV, and the external quantum efficiencies (EQEs) of perovskite light-emitting diodes (LEDs) have reached 26.4% (blue light), 32.5% (red light), and 31% (green light), respectively. Despite their high optoelectronic potential, surface defects and grain boundaries in perovskite polycrystalline films remain key barriers to performance improvement and commercialization. In contrast, single-crystal perovskites, characterized by minimal grain boundaries and low defect densities, emerge as superior candidates for high-performance optoelectronic devices. They also serve as an ideal platform for investigating and elucidating the intrinsic properties of perovskite materials. Therefore, this review outlines recent progress in perovskite single-crystal crystallization, properties, fabrication and applications, clarifies intrinsic structure–property and growth-defect relationships, advances a device-demand-driven material design concept, and offers critical insights into challenges, prospects and future commercialization. We believe that this review will provide valuable insights and inspiration for future research endeavors in this domain.

1. Introduction

Perovskite materials, initially defined as calcium titanate ($CaTiO_3$) discovered by Gustav Rose in 1839 and named after the Russian mineralogist Lev Perovski, have evolved into a broad class of compounds with the general formula ABX_3 and a crystal structure analogous to $CaTiO_3$.[1–3] In terms of the formula, symbol A represents a monovalent cation with a large ionic

---

[a] Key Laboratory of Advanced Materials Chemistry and Devices (AMCD Lab) of the Department of Education of Inner Mongolia Autonomous Region, College of Chemistry and Environmental Science, Inner Mongolia Normal University, Hohhot, 010022, P. R. China. E-mail: zilu@imnu.edu.cn; zxj@imnu.edu.cn

[b] Henan Engineering Research Centre of Building-Photovoltaics of Mathematics and Physics College, Henan University of Urban Construction, Pingdingshan, 467036, P. R. China

[c] Key Laboratory of New Energy and Rare Earth Resource Utilization of State Ethnic Affairs Commission, Key Laboratory of Photosensitive Materials & Devices of Liaoning Province, School of Physics and Materials Engineering, Dalian Minzu University, 18 Liaohe West Road, Dalian, 116600, P. R. China. E-mail: xuwen@dlnu.edu.cn

---

Lu Zi

Lu Zi received her PhD from Jilin University in June 2023. Currently, she works at the College of Chemistry and Environmental Science at Inner Mongolia Normal University. Her research focuses on solution-processed perovskite single crystals and the design optimization of related functional optoelectronic devices.

Ximan Fan

Ximan Fan earned a BS in Chemistry from Baotou Teachers College, Inner Mongolia University of Science and Technology. Currently, she is a masters student at Inner Mongolia Normal University under the supervision of Prof. Gejihu De. Her research interests focus on luminescent materials.

radius (*e.g.*, inorganic cations such as Cs^+ and Rb^+, or organic cations such as methylammonium and formamidinium), symbol B is a small-radius bivalent metal cation such as Ge^{2+} or Sn^{2+} or Pb^{2+}, and symbol X corresponds to a halide anion (*e.g.*, chloride, bromide or iodide ions).[4–6] The diverse combinations of A, B, and X elements with varying ionic radii enable perovskites to adopt multiple crystal structures, including high-symmetry cubic (*Pm*3*m* space group), tetragonal, and low-symmetry orthorhombic phases. The cubic phase, characterized by corner-sharing BX_6 octahedra with B cations at the center and AX_{12} cuboctahedra enclosing A cations, is regarded as the most optimal crystal structure. It is precisely the unique crystal structure of perovskite that makes it have special physical and chemical properties.[7–11]

Perovskite, a semiconductor material, has been widely applied in photovoltaics, photodetectors, light-emitting diodes, and lasers due to its high absorption coefficient, carrier mobility, defect tolerance, long carrier diffusion length and lifetime.[12–20] Over the past decade, perovskite-based photoelectric devices have attracted widespread attention from researchers worldwide due to their promising test results. Notably, the certified power conversion efficiency (PCE) of perovskite solar cells has surged from 3.8% to 26.95%, underscoring their immense commercial potential.[21–30] However, this PCE remains below the theoretical Shockley–Queisser limit of 30.5%, primarily due to grain boundaries and surface defects inherent in microcrystalline or polycrystalline perovskite films.[31–36] In contrast, single-crystal perovskites with few defects and grain boundaries demonstrate superior optoelectronic properties and stability. These advantages not only provide an ideal platform for investigating the intrinsic characteristics of perovskite materials but also hold promise for the development of high-performance optoelectronic devices.[37–47] Despite their great potential in optoelectronics, research on single-crystal perovskites has been slow to progress because of a late start, and only a handful of research groups are currently working on them. Although recent years have seen an increase in publications on single-crystal perovskites, comprehensive reviews summarizing their growth methods, properties, and applications remain scarce.[48–54] Therefore, reviews that summarize the recent advances and challenges in the growth, properties, and applications of single-crystal perovskite materials are urgently required.

Based on the above, this review aims to present a comprehensive and detailed overview of the current development in single-crystal perovskites. We have expounded upon the foundational properties inherent to single-crystal perovskites, carried out a thorough examination of diverse crystal growth

Le Liu

Le Liu is currently a lecturer at the College of Mathematics and Physics, Henan University of Urban Construction. She received her doctoral degree in Microelectronics and Solid-State Electronics from Jilin University in 2022. Her research focuses on perovskite solar cells.

Xiaojuan Zhuang

Xiaojuan Zhuang received her masters degree from Inner Mongolia Normal University in June 2002. Currently, she is an associate professor at the College of Chemistry and Environmental Science at Inner Mongolia Normal University. Her research interests focus on the design and synthesis of novel organic optoelectronic functional materials.

Shuna Guan

Shuna Guan earned her BS degree from Cangzhou Normal University. Currently, she is a masters student at Inner Mongolia Normal University under the supervision of Prof. Gejihu De. Her research interests focus on luminescent materials.

Wen Xu

Wen Xu earned his BS degree in 2009 and received his PhD in 2014 from Jilin University. From 2015 to 2018, he worked as a research fellow at Nanyang Technological University, and a JSPS research fellow at Tokyo Institute of Technology, respectively. Currently, he is a full professor at the School of Physics and Materials Engineering Dalian Minzu University. His research interests focus on luminescent materials, plasmonics and photoelectric devices.

methodologies employed in their synthesis, complete with an assessment of the unique benefits each technique offers. Additionally, we provide a consolidated summary of their main application areas. Finally, this review delves into the prevailing challenges confronting single-crystal perovskites and contemplates potential avenues for their future development.

2. Brief introduction to single-crystal perovskites

In this section, the crystal structures and fundamental properties of single-crystal perovskite materials are comprehensively summarized. These distinctive characteristics serve as the primary underpinnings for the superior photoelectric performance and enhanced stability exhibited by single-crystal materials compared to microcrystalline or polycrystalline thin films.

2.1. Crystal structure of perovskites

In 1926, Goldschmidt described the crystal structure of perovskites when studying the tolerance factor.[55] It was not until the 1950s that the perovskite structure derived from X-ray data of barium titanate was reported.[56] Generally, the perovskite structure consists of an octachedral network of halide metals and a void portion formed by larger monovalent cations. The matching combination of these portions causes the diversity of the perovskite structure. Depending on the dimensionality, they mainly include zero-dimensional (0D), one-dimensional (1D), rarely reported two-dimensional (2D), and widely studied three-dimensional (3D) perovskite materials. Therefore, we will mostly discuss the 3D perovskites (Fig. 1a). As mentioned before, the ABX_3 perovskite structure is formed by a 3D network, with A-site species located in the void of corner-sharing BX_6 octahedra.[57–63] While the 3D network structure demonstrates flexibility arising from the large gap, its formation through random combinations is not permissible. In order to maintain crystallographic stability, the ionic radii of A, B, and X must correspond to the formulae:[64]

$$t = \frac{(r_A + r_X)}{\sqrt{2}(r_B + r_X)} \tag{1}$$

$$\mu = \frac{r_B}{r_X} \tag{2}$$

where t and μ are the tolerance factor and octahedral factor, respectively. For halide perovskites, $0.81 \le t \le 1.11$ and $0.44 \le \mu \le 0.90$ are the most ideal values for forming a stable perovskite structure. The ideal cubic perovskite structure can be formed if t is in the range of 0.9 to 1.0, and the distorted perovskite structure can be obtained when t lies in the range 0.7–1.0. The ilmenite structure perovskite will be formed when $t > 1$, whereas the two-dimensional perovskite will be obtained when $t < 0.7$ (Fig. 1b).[65]

2.2. Performance of single-crystal perovskites

Currently, the development of optoelectronic devices predominantly centers on polycrystalline thin film perovskite materials. Despite the remarkable achievements attained thus far, several inherent issues associated with polycrystalline perovskites are unavoidable. These include the reduction of carrier mobilities, electron–hole recombination, material instability, and hysteresis in the current-density voltage (*J*–*V*) curves, which are primarily attributed to the presence of grain boundaries and surface defects in polycrystalline perovskites. Consequently, single-crystal perovskites, characterized by lower trap-state densities, longer diffusion lengths, and higher carrier mobilities, emerge as the ideal candidates for investigating the intrinsic properties of perovskite materials. Furthermore, they hold significant promise for driving breakthroughs in device performance.[66–68]

2.2.1. **Stability.** Stability, a critical physical parameter of perovskite materials, is a major factor restricting their commercialization. Specifically, polycrystalline perovskite thin films exhibit poor ambient stability and high sensitivity to moisture, oxygen, light and heat, which are attributed to the presence of grain boundaries. These grain boundaries are widely recognized as the initial sites of material decomposition: they contain a thin amorphous intergranular layer (more moisture-sensitive than crystalline regions), and their weak crystallinity causes rapid moisture-induced degradation along the boundaries. Additionally, they also act as channels for the thermally induced volatilization of organic iodides. Therefore, an increasing number of researchers are committed to improving the stability of polycrystalline perovskite thin film materials by increasing the formation energy, including the

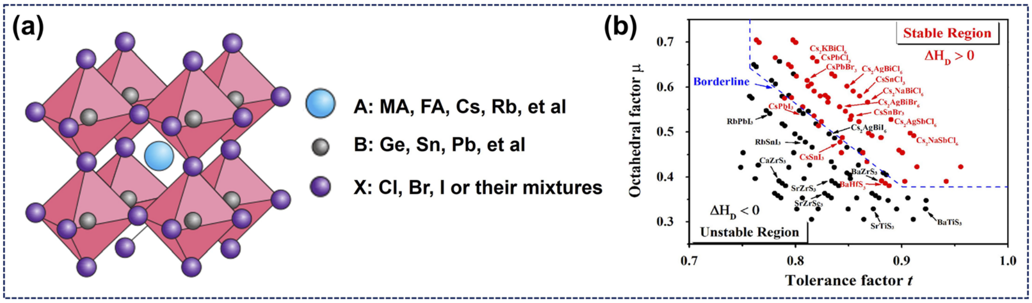

Fig. 1 The crystal structures, tolerance and octahedral factors of perovskite-type materials: (a) crystal structure of 3D perovskites.[63] Copyright 2014, Springer Nature. (b) Tolerance factor–octahedral factor map of 138 perovskite compounds, where red dots represent stable phases and black dots represent unstable phases.[65] Copyright 2017, American Chemical Society.

design of 2D perovskite structures and the introduction of additives. For example, Smith *et al.* reported that a device with parts of MA$^+$ ($CH_3NH_3^+$) replaced with PEA ($C_6H_5CH_2CH_2NH_3^+$) is more resistant to moisture and can be fabricated under humid conditions. Li *et al.* showed that alkylcarboxylic acid ω-ammonium additives as templates can improve the moisture stability of perovskite solar cells. Although tremendous efforts have been devoted to enhancing device stability by reducing grain boundaries and defects, current polycrystalline perovskite thin films still fall short of meeting the requirements for highly efficient devices with long-term stability. In comparison, single-crystal perovskites exhibit a perfectly long-range ordered ABX_3 crystal structure with highly regular atomic arrangements, which nearly eliminates the grain boundaries, dislocations, voids, and other defects ubiquitous in polycrystalline counterparts. This low defect, grain-boundary-free architecture drastically diminishes reactive sites, impeding the inward diffusion and infiltration of erosive agents while suppressing the preferential cleavage of ionic bonds at defect loci, thereby endowing the material with significantly enhanced resistance to moisture and oxidation.[69–74] Thus, the single-crystal perovskite materials not only maintain the basic physical parameters of polycrystalline counterparts but also exhibit superior stability owing to the absence of grain boundaries. Taking $MAPbI_3$ as an example, Tao *et al.* proposed that the centimeter-sized $CH_3NH_3PbI_3$ ($MAPbI_3$) single crystal shows obvious excellent photoelectric performance and thermal stability compared to polycrystalline films. Meanwhile, Huang *et al.* observed that the $MAPbI_3$ single crystals synthesized 2–3 years prior, when stored in an ambient atmosphere without any encapsulation, retained their black color and shiny crystal facets with no significant degradation (Fig. 2a and b). The $MAPbI_3$ crystals exhibited relatively good thermal stability, as evidenced by thermogravimetric analysis. Specifically, the decomposition temperature of single-crystal samples (240 °C) is higher than those of their polycrystalline thin film counterparts (150 °C). Additionally, Dong *et al.* fabricated lateral-structure perovskite solar cells (PSCs) based on $MAPbI_3$ single crystals by a simple MAI treatment procedure. The test results demonstrated that these devices exhibit excellent long-term operational stability, with no significant degradation observed after continuous operation for 200 hours (Fig. 2c). Subsequently, Yang *et al.* reported that a mass loss of the $FAPbI_3$ single crystal occurred at 320–360 °C, which means the thermal stability of the $MAPbI_3$ single crystal is lower than that of the $FAPbI_3$ single crystal (Fig. 2d and e). Recently, $(FAPbI_3)_{0.9}(MAPbBr_3)_{0.05}(CsPbBr_3)_{0.05}$ single crystals with long-term stability against water–oxygen were prepared. This work provides a single-crystal-based paradigm for long-

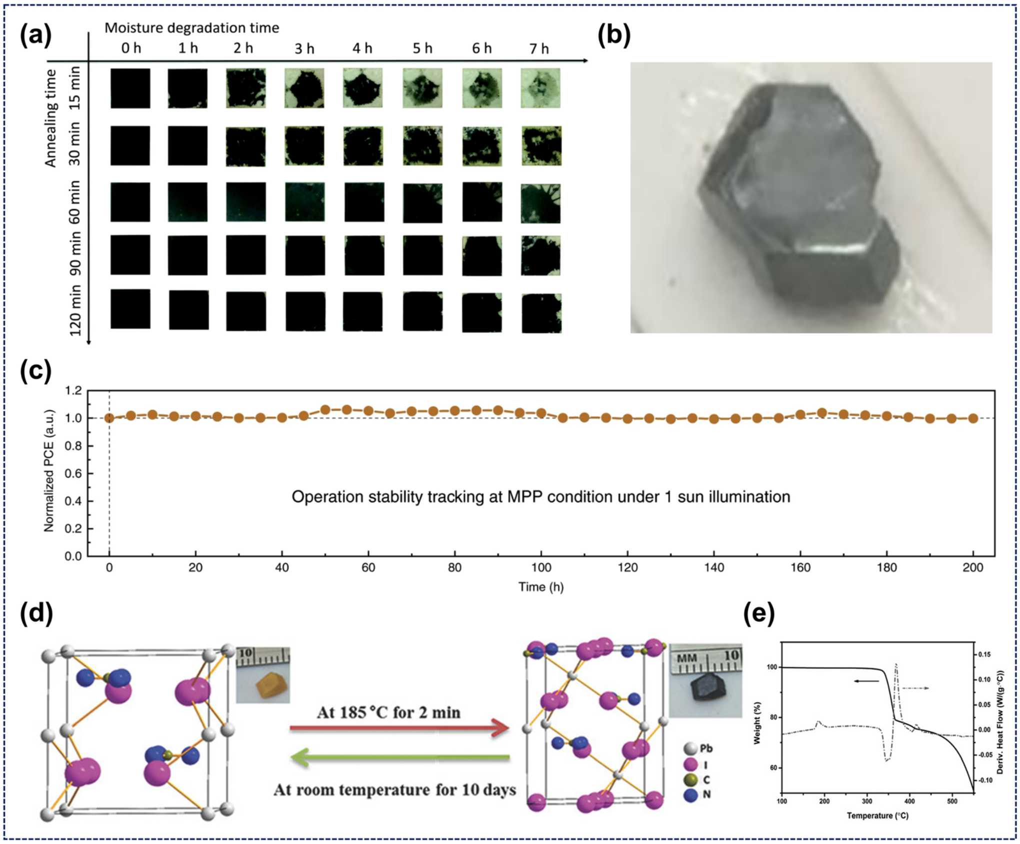

Fig. 2 Stability of perovskite materials: (a) photographic images recorded the degradation process of $MAPbI_3$ polycrystalline thin films at 85% humidity; (b) photograph of an $MAPbI_3$ single crystal stored in air without encapsulation for more than two years.[78] Copyright 2017, Royal Society of Chemistry. (c) Long term stability of the lateral-structure $MAPbI_3$ single-crystal device.[75] Copyright 2020, Springer Nature. (d and e) TGA–DSC curves and transformation of the phase structure of the $FAPbI_3$ single crystal.[79] Copyright 2016, Wiley-VCH.

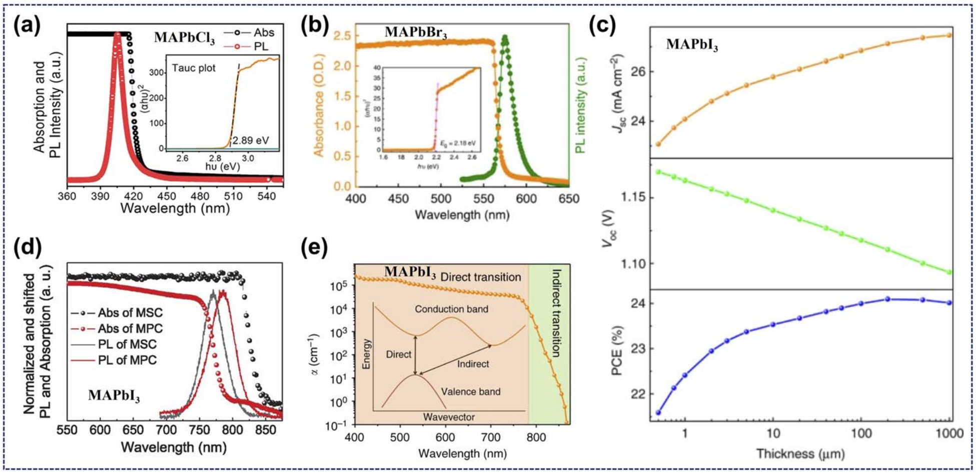

Fig. 3 Optical properties of single crystal perovskites: (a and b) light absorption and photoemission spectra of $MAPbCl_3$ and $MAPbBr_3$ single crystals.[81,87] Copyright 2019, American Chemical Society. Copyright 2015, Springer Nature. (c) Calculated ideal dependence of PCE, J_{SC} and V_{OC} of single crystal solar cells on thin single-crystal thickness; (d) comparison of light absorption and photoemission spectra between $MAPbI_3$ single crystal and its polycrystalline counterpart; (e) schematic of direct/below-bandgap transitions and absorption coefficient of polycrystalline $MAPbI_3$ thin film.[84,91] Copyright 2017, Springer Nature. Copyright 2015, The American Association for the Advancement of Science.

term stability studies from the perspective of the intrinsic structure.[75–80]

2.2.2. Photoabsorption properties. Compared with traditional semiconductors, perovskite semiconductors possess a higher optical absorption coefficient, which is very beneficial for diminishing the thickness of thin film materials employed in fabricating photoelectric devices. The approximately 500 nm thick polycrystalline thin films could achieve absorption in the entire visible spectrum. Distinct from polycrystalline thin films, single-crystal perovskites exhibit a broader light absorption range, stemming from their notable indirect-bandgap absorption. This unique absorption can be further explained by the distinct below-bandgap absorption in thick single-crystal materials (negligible in polycrystalline films). Moreover, the above-gap transition absorption coefficient is orders of magnitude higher than the below-bandgap counterpart This is largely due to the long-range ordered lattice of single crystals, which diminishes defects and non-radiative recombination, cuts absorption energy loss, and realizes superior absorption efficiency. As a typical example, previous studies on $MAPbI_3$ have demonstrated that the energy of its indirect-bandgap absorption transition is 60 meV lower than that of the direct bandgap transition, and this difference accounts for its below-bandgap absorption.[81–85] For example, the absorption onsets of $MAPbCl_3$, $MAPbBr_3$, and $MAPbI_3$ single crystals are 430 nm, 570 nm, and 850 nm, respectively, whereas those of their thin film counterparts are approximately 407 nm, 550 nm, and 780 nm, respectively. This results in a long-wavelength shift of the absorption edge relative to the corresponding polycrystalline perovskite thin films. The photoluminescence peaks of these single crystals occur at wavelengths lower than their absorption onsets, which is attributed to the coexistence of direct and indirect band gaps.[86–88] It has been reported that the shift of $MAPbI_3$ single crystals is the major concern during these redshifts. This is attributed to two reasons primarily: one is the optical band gap of $MAPbI_3$ (1.5 eV) being close to the bandgap of the optimal photovoltaic material, another is the increase of power conversion efficiencies in $MAPbI_3$-based solar cells due to the upper limit of short-circuit current density caused by the redshift. Additionally, Huang *et al.* found that the carrier diffusion length of $MAPbI_3$ single crystals was 175 ± 25 μm under 1 sun, which was suitable for the direct application of X-ray and gamma ray sensing.[89–91] Liu *et al.* reported that the optical absorption of the $MAPbI_3$ single crystal wafer can expand to 910 nm, which approximately shifted 110 nm compared to the thin film material (Fig. 3).[92]

2.2.3. Carrier transport properties. Electronic properties are among the important parameters for modeling photovoltaic and optoelectronic devices. Research shows that the high trap-state densities and defects in polycrystalline thin films provide recombination centers for charge carriers, thereby seriously decreasing their carrier lifetime and diffusion length. In contrast, bulk single crystals feature a tightly packed crystal structure, which minimizes grain boundaries and surface defects, and is conducive to enhancing the lifetime and diffusion length of charge carriers (Fig. 4). Additionally, the crystal symmetry of the ABX_3 architecture in single-crystal perovskites governs carrier effective mass and migration paths. In high-symmetry lattices with well-ordered atomic configurations, migrating carriers experience negligible potential field fluctuations, translating to reduced effective mass and smooth transport. Meanwhile, varying degrees of lattice distortion alter carrier scattering patterns and migration channels, whereas the intrinsic low distortion characteristic of single crystals alleviates migration impediments and boosts transport efficiency. For instance, Beard *et al.* reported that the surface recombination velocity of $MAPbBr_3$ single crystals was $3.4 \pm 0.1 \times 10^3$ cm s^{-1}, several orders in magnitude lower than that of important unpassivated semiconductors.[93,94] Therefore, compared with polycrystalline thin films, single crystals with lower charge trap

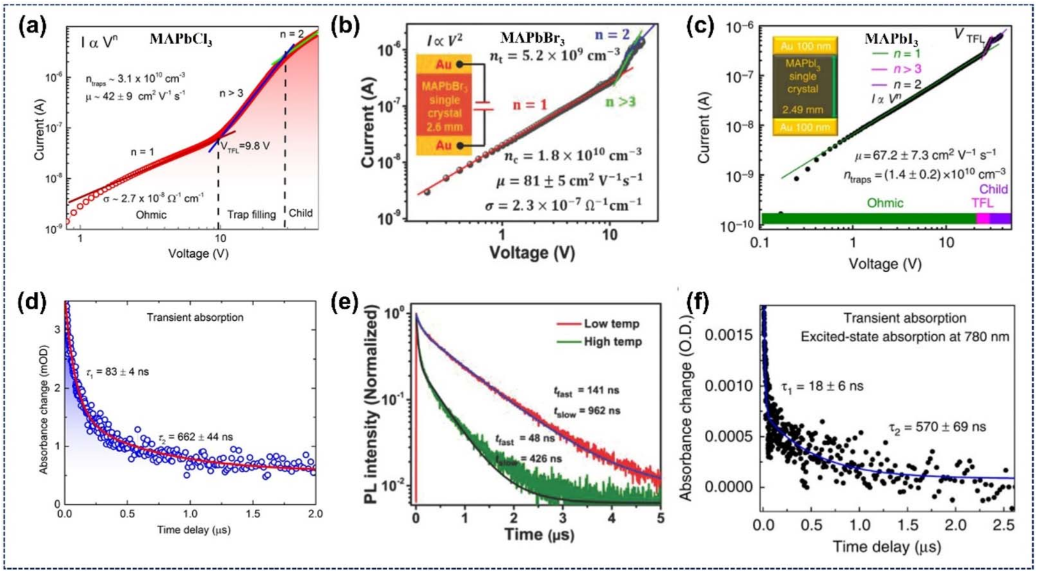

Fig. 4 The carrier characteristics of single crystal perovskites: (a and b) transient absorption and *I*–*V* response of the $MAPbCl_3$ single crystal; (c and d) *I*–*V* trace and a comparison of PL time-decay trace for $MAPbBr_3$ single crystals; (e and f) *I*–*V* response and transient absorption of the $MAPbI_3$ single crystal.[54,81,122] Copyright 2015, American Chemical Society. Copyright 2018, Wiley-VCH. Copyright 2015, Springer Nature.

densities, higher carrier mobilities, longer diffusion lengths and carrier lifetime are better candidates for high performance optoelectronic applications. As shown in Table 1, Bakr *et al.* prepared $MAPbX_3$ (X = Br, I) single crystals and found exceptionally low trap-state densities on the order of 10^9 to 10^{10}, several orders in magnitude lower than that of their thin film counterparts.[86,95] Huang *et al.* reported that bulk carrier diffusion length exceeded 175 μm under 1 sun illumination and even exceeded 3 μm under weak light, which outdistanced that of the polycrystalline thin films.[91] Zhang *et al.* found that the diffusion lengths of $MAPbI_{3-x}Cl_x$ ($x = 0.005$) exceeded 380 μm under 1 sun illumination, approximately two times higher than that of $MAPbI_3$ single crystals.[96] The difference in values given is

Table 1 Summary of single-crystal perovskite performance parameters

Sample	Trap density [10^{10} cm^{-3}]	Mobility [cm^2 V^{-1} s^{-1}]	Carrier lifetime fast	slow [ns]	Technique	Diffusion length [μm]	Ref.
$MAPbCl_3$	3.1	42	83	662	SCLC	8.0–8.5	122
$MAPbCl_3$	0.79	64	—		SCLC	—	87
$MAPbCl_3$	—	179	—		Hall	—	103
$MAPbBr_3$	2.6 (Hole) 11 (Electron)	4.36 —	—		Hall	—	103
$MAPbBr_3$	0.67	83.9	132	897	SCLC	5.3–13.8	46
$MAPbBr_3$	0.62	81	139	899	SCLC	5.4–14.2	54
$MAPbBr_3$	20	60	189		Hall	5	95
$MAPbBr_3$	0.58	115 20–60 38	41	357	TOF Hall SCLC	3–17	86
$MAPbBr_3$	0.65 (Electron) 0.44 (Hole)	—	997		SCLC	—	37
$MAPbBr_3$	3	24	28	300	SCLC	1.3–4.3	81
$MAPbI_3$	0.18 (Hole) 4.8 (Electron)	34	—		Hall	—	103
$MAPbI_3$	3.3	2.5	22	1032	SCLC	2–8	86
$MAPbI_3$	1.4	67.2	18	570	SCLC	1.8–10.0	81
$MAPbI_3$	3.6 (Hole) 34.5 (Electron)	164 ± 25 105 ± 35	82 ± 5 μs (TPV) 95 ± 8 μs (IS)		SCLC Hall	175 ± 25	91
$MAPbI_{3-x}Cl_x$ ($x = 0.005$)	3.4 ± 1.5	70	489 ± 221 μs (IS)		SCLC	380 ± 40	96

mainly caused by different transport processes as revealed by measurement methods.

2.2.4. **Bandgap engineering.** Spectral tunability stands as one of the most distinctive fundamental properties of perovskite crystal materials. Research shows that organic–inorganic hybrid perovskites are highly suitable for photovoltaic applications, as their bandgap can be tuned to the 1.0–1.7 eV range by modifying the compositions of organic cations and inorganic anions. In other words, the ABX_3 lattice structure of single-crystal perovskites exhibits exceptional tunability, enabling precise modulation of bond lengths and angles between X site halide ions and A/B-site cations through ion doping or component regulation. These geometric variations in bonding directly influence the electronic band structure, thereby allowing fine-tuned control over the bandgap width.[97–99,106] Currently, there are usually two efficient ways of bandgap tuning, one is to change the type and number of halogen atoms in ABX_3 perovskites. In 2015, Huang *et al.* reported that $MAPbBr_{3-x}Cl_x$ and $MAPbI_{3-x}Br_x$ mixed halide perovskite single crystals with continuous tuning in the visible range could be applied in the narrowband photodetection (Fig. 5a–c).[100] Then, Liu *et al.* prepared $MAPb(Br_xI_{1-x})_3$ ($x = 0$–1) single-crystal perovskites and found that the absorption spectrum of samples could shift in the wavelength range from green to red by changing the Br content in the single crystals (Fig. 5d–f).[101] Han *et al.* reported that the $MAPbI_{3-x}Br_x$ (I/Br = 10 : 1 in the precursor) single crystals had a long carrier lifetime of up to 262 μs under 1 sun illumination, approximately two times longer than that of $MAPbI_3$ single crystals.[102] The other is to change the type and size of organic cations. As reports show, the bandgap values of

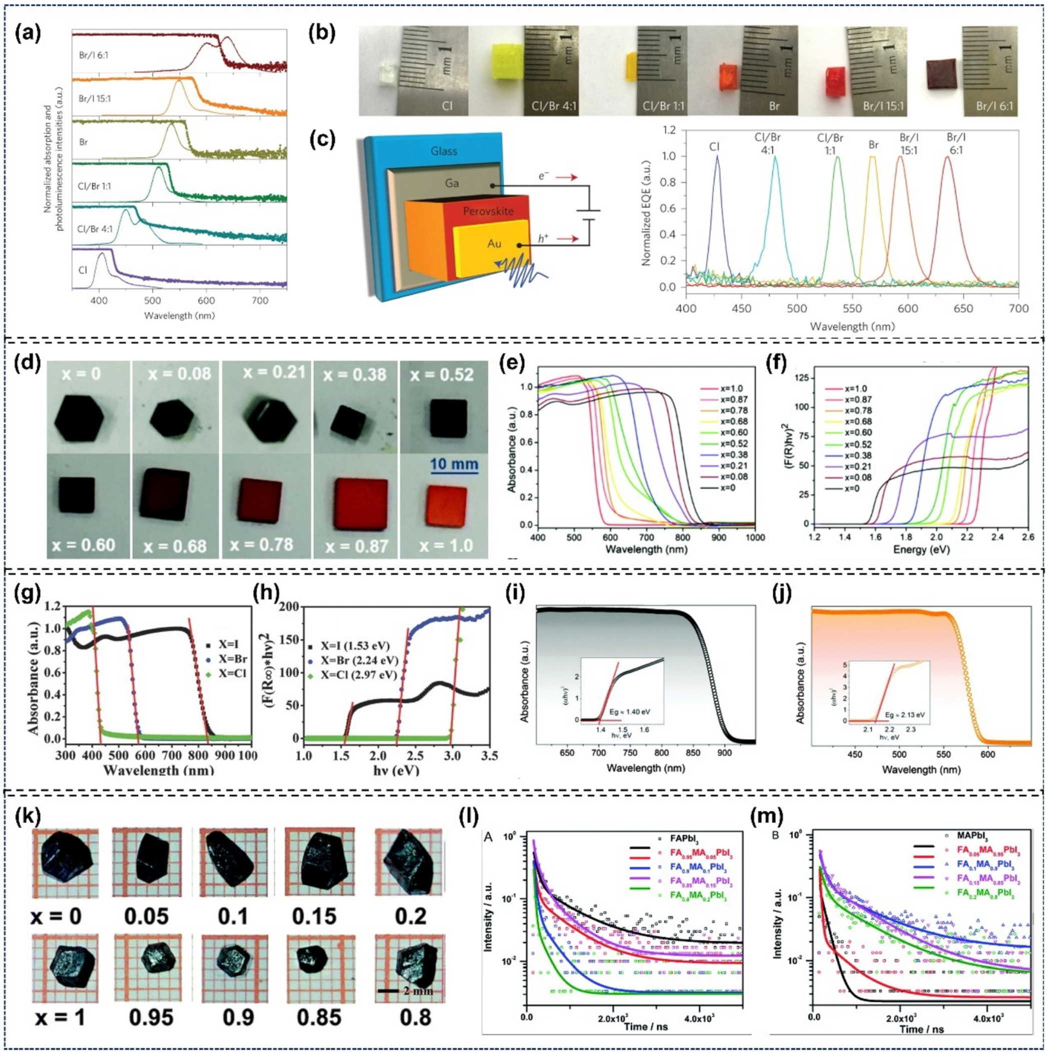

Fig. 5 Properties of hybrid halide perovskite single crystal materials: (a–c) photographs, corresponding bandgap, absorption and photoluminescence spectra of $MAPbBr_{3-x}Cl_x$ and $MAPbI_{3-x}Br_x$ mixed halide perovskite single crystals.[100] Copyright 2015, Springer Nature. (d–f) Photographs, Vis-NIR absorption spectrum and bandgap of $MAPb(Br_xI_{1-x})_3$ ($x = 0$–1) single-crystal perovskites.[101] Copyright 2016, Royal Society of Chemistry. (g and h) UV-vis-NIR absorption spectrum and bandgap of $MAPbX_3$ (X = Cl, Br, I) single crystals.[103] Copyright 2015, Wiley-VCH. (i and j) Absorption spectrum and Tauc plots of $FAPbX_3$ (X = Br, I) single crystals.[104] Copyright 2015, Royal Society of Chemistry. (k–m) Photographs and time-resolved photoluminescence spectra of $FA_{(1-x)}MA_xPbI_3$ (top: $x = 0$–0.2, bottom: $x = 1$–0.8) single crystals.[105] Copyright 2017, Royal Society of Chemistry.

$MAPbCl_3$, $MAPbBr_3$, and $MAPbI_3$ single crystals are 2.97, 2.24, and 1.53 eV, respectively (Fig. 5g and h), and that of $FAPbBr_3$ and $FAPbI_3$ single crystals are 2.13 and 1.4 eV, respectively (Fig. 5i and j).[103,104] In 2017, Zhou *et al.* synthesized a series of $FA_{(1-x)}MA_xPbI_3$ ($x = 0$–0.2, 0.8–1) single crystals and found that the carrier lifetime of $FA_{(1-x)}MA_xPbI_3$ ($x = 0.8$–0.95) was longer than that of $MAPbI_3$ (Fig. 5k–m).[105] In addition, theoretical calculations show that the change of divalent cation is also responsible for the reduction of the bandgap.[106]

2.2.5. Low ion migration and defect density. Electronic trap states play a pivotal role in the performance aging of perovskite optoelectronic devices, such as solar cells. In single-crystalline perovskite-based optoelectronic devices, these electronic trap states are primarily derived from bulk defects and surface defects within the material.[5] Bulk defects predominantly arise during the growth of single crystals *via* low-temperature solution-based methods. Specifically, excessive temperature-dependent variations in the precursor solution concentration leads to uneven growth rates of the crystal across different time periods and crystal planes, thereby forming point defects such as Pb vacancies and I vacancies, which ultimately increase the bulk defect density.[107,108] Surface defects are mainly caused by the erosion of the single crystal surface by solvents. Upon retrieval of the crystal from the growth solution, temperature fluctuations perturb the dissolution equilibrium (MAI > PbI_2 in solubility). This perturbation triggers an imbalance in the surface composition, thereby inducing the formation of surface defects, leading to MA vacancies and Pb-enriched surfaces.[84,91]

To effectively suppress bulk defects in single crystals, the key is to scientifically and rationally regulate the crystal growth environment. Employing a slow heating or cooling method to reduce temperature change rate, which can mitigate fluctuations in the low-temperature crystallization environment and slow crystal growth, significantly minimizes the formation of various defects. For example, Liu *et al.* prepared high-quality $MAPbBr_3$ single crystals *via* slow low-temperature gradient crystallization (25–60 °C). Compared with crystals grown at high temperatures (100 °C), the bulk defect density of these crystals decreased by approximately one order of magnitude, enabling the fabrication of high-performance photodetectors.[54] Subsequently, they further employed a dynamic flow microreactor system for the growth of ultrathin single-crystal wafers with controllable properties. Results showed that the external circulation continuously supplied precursor solution for crystal growth, maintained uniform solution concentration and a stable growth environment, and yielded $MAPbI_3$ single crystals with high crystallinity and low trap density (6×8^{10} cm^{-3}).[48] Despite progress in controlling bulk defects, surface defects remain unavoidable due to solvent damage when crystals are retrieved from the solution. Reports indicate that the defect density near the crystal surface is several orders of magnitude higher than that in the bulk. Huang *et al.* observed distinct interfaces between two crystal layers by inducing discontinuous single crystal growth, and found significantly increased defect density at these interfaces, confirming that crystal surfaces contain more defects than the bulk.[109] Surface defects in single crystals are typically passivated through chemical modification, physical coating, elemental doping, and interface engineering approaches. Huang *et al.* achieved a high-performance single-crystalline perovskite solar cell by coating a layer of MAI on the surface of $MAPbI_3$ single crystals, with a PCE of up to 17.8%.[84]

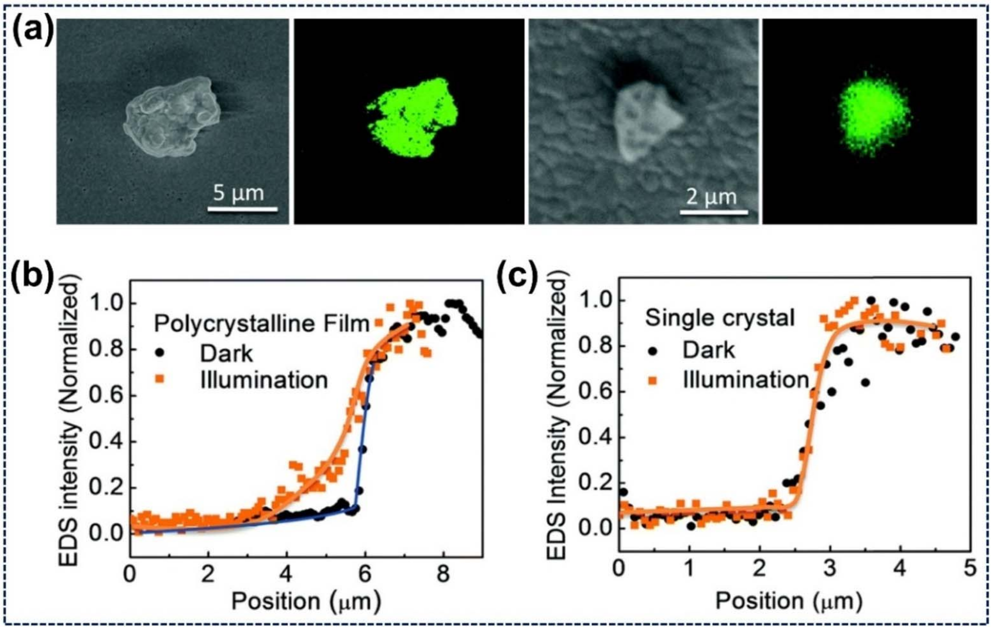

Fig. 6 EDS study on Br^- diffusion in $MAPbI_3$: (a) SEM and EDX Br-element distribution images of a $PbBr_2$ particle (without/with illumination); (b and c) Br-element line scans of $MAPbI_3$ polycrystalline film and single crystal (without/with illumination).[116] Copyright 2016, Royal Society of Chemistry.

Meantime, Bakr *et al.* reduced the growth temperature of single crystals using a mixed solvent, significantly suppressing the thermal decomposition of MAI on the $MAPbI_3$ surface and achieving a PCE of 21.9% for single-crystalline perovskite solar cells.[110]

Perovskites, a class of ionic crystals with a soft lattice structure, undergo ion migration under external stimuli. When an electric field is applied to the perovskite layer, it not only enables hole/electron transport but also triggers the redistribution of mobile ions and defects (*e.g.*, vacancies, interstitial ions).[111,112] While perovskite ion migration involves both anions (*e.g.*, I^-, Br^-) and cations (*e.g.*, MA^+, Pb^{2+}), experimental and theoretical studies consistently confirm that in lead-based perovskites, iodide ions dominate the overall migration process due to their substantially lower migration activation energy and higher diffusion coefficient than other mobile ions. Ion migration imposes critical challenges to device performance: it alters the internal electric field distribution of the device, complicating the accuracy of device characterization. More importantly, it directly induces the photocurrent hysteresis effect, and accelerates both the decomposition of perovskite materials and the degradation of device performance.[113,114] Studies on switchable photovoltaic effects conducted by Huang *et al.* have provided key insights into this phenomenon. Their research revealed that ion migration in polycrystalline perovskite films is likely dominated by grain boundaries. The conclusion arrived at was that devices based on large-grain films exhibit significantly higher switching difficulty compared to those with small-grain films.[115] Additionally, they observed Br^- diffusion (from $PbBr_2$) in $MAPbI_3$ polycrystalline films, whereas no such diffusion was detected in $MAPbI_3$ single crystals (Fig. 6a–c). This result further confirms that grain boundaries serve as fast channels for ion migration.[116] In contrast to polycrystalline films with dense grain boundaries, single-crystal perovskites have a long-range ordered, low-defect lattice with well-regulated atomic coordination. This intrinsic structural advantage not only eradicates the primary pathways for ion migration but also elevates vacancy formation energy, thereby achieving remarkable suppression of ion migration. Additionally, B site cations in single crystals form stable octahedral coordination with X site halides, anchoring halide ions and reducing their tendency to escape the lattice. Consequently, this not only ensures the stable performance of fabricated devices but also alleviates ion migration induced damage to perovskite materials.[59,82]

3. Single crystal growth methods

The properties of materials largely depend on their preparation methods. The performance of single-crystal materials is closely associated with their crystal quality, with higher quality yielding superior performance.[117] Therefore, understanding the nucleation and growth mechanisms is crucial for developing more high-quality single-crystal perovskites. Similar to the growth mechanisms of other single-crystal materials, perovskite crystallization typically involves nucleation and growth. The difference lies in that perovskite crystallization can occur in solution, vapor, or molten systems. Generally, nucleation can be categorized into homogeneous nucleation and heterogeneous nucleation. Homogeneous nucleation refers to the spontaneous nucleation process without preferential nucleation sites, featuring the uniform formation of crystal nuclei in the mother liquor. That is to say, it occurs when components across the entire mother phase nucleate to generate a stable second phase without being influenced by impurities or external surfaces, and it is considered a thermodynamic process in nature.[25,81] According to the classical nucleation theory, the nucleation rate (J) follows the Arrhenius-type equation below:[19]

$$J = K \exp\left(-\frac{\Delta G^*}{k_B T}\right) \tag{3}$$

where K is a constant related to supersaturation concentration, ΔG^* represents the nucleation barrier or Gibbs free energy change in nucleation, k_B is the Boltzmann constant, and T stands for thermodynamic temperature. In contrast, heterogeneous nucleation is more prone to take place at preferential

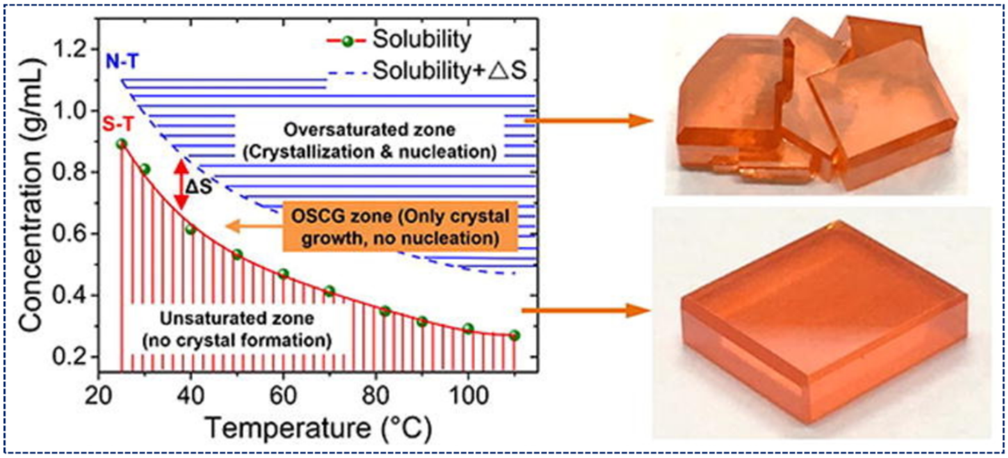

Fig. 7 Solubility curves of different regions in the single-crystal growth model, concentration–growth temperature relationship, and photos of $MAPbBr_3$ single crystal samples from distinct growth regions.[46] Copyright 2019, Elsevier.

nucleation sites including phase interfaces, surfaces, or impurities, as stable nucleation surfaces are provided there. The selection of the nucleation process is determined by the requirements of different application fields, and the desired crystal size can be controlled accordingly.

Fig. 7 shows the solubility curves corresponding to typical solution-based crystal growth methods, including inverse temperature crystallization, antisolvent crystallization, and volatile solvent crystallization. The horizontal axis stands for the crystal growth driving force (temperature variation), and the vertical axis for solution concentration. The crystallization process of perovskite crystals can be delineated by the solubility curve (S–T curve) and the nucleation curve (N–T curve) of the perovskite solution.[46] Changes in the driving force trigger the system to transition among three distinct regions: the dissolution zone (crystal dissolution), the growth zone (steady crystal growth), and the nucleation zone (rapid crystallization). Since crystal growth requires a saturated growth solution, no crystallization or crystal growth takes place in the region below the S–T curve due to the unsaturated state of the perovskite precursor solution. Once the solution temperature surpasses the threshold defined by the S–T curve, the growth solution becomes saturated, allowing perovskite crystals to grow. As the temperature rises further, the solution moves into the supersaturation region above the N–T curve, where continuous energy supply surmounts the nucleation energy barrier and triggers crystal nucleation in the solution. However, the high energy level in this region tends to induce defects and twins in perovskite crystals, which renders it unsuitable for the sustained growth of single-crystal perovskites. Stringent regulation of crystal growth driving forces (temperature, solute concentration, and solution volume) is critical to avoiding adverse effects like crystal dissolution and unintended nucleation, which tend to cause grain boundaries and core stacking in the final crystalline products. Tiny driving force fluctuations can push the system out of the optimal growth region, particularly for narrow growth zone materials. For example, the 0.005 M solubility and super-solubility difference of inverse temperature crystallization grown $FAPbBr_3$ crystals demands stringent temperature and concentration regulation.[11] In addition, the growth rate of single-crystal perovskites is closely correlated with the temperature of the growth solution. Given the inherent limitations of solute transport in the growth solution, an excessively high growth rate is also detrimental to the preparation of high-quality single-crystal perovskites.

The kinetics of nucleation and growth are intricately governed by factors such as the degree of supersaturation, temperature, and the surface free energy of the substrate, all of which play pivotal roles in determining the final morphology and quality of the perovskite crystals. Extensive efforts have been devoted to the fabrication of high-quality single-crystal perovskites *via* the optimization of growth solution parameters. Depending on the morphology of the obtained single-crystal perovskite materials, these crystal growth techniques can be broadly classified into three categories: bulk crystal techniques, thin crystal techniques, and single crystal nanostructure techniques.[118–140] In this section, bulk crystal techniques are introduced emphatically.

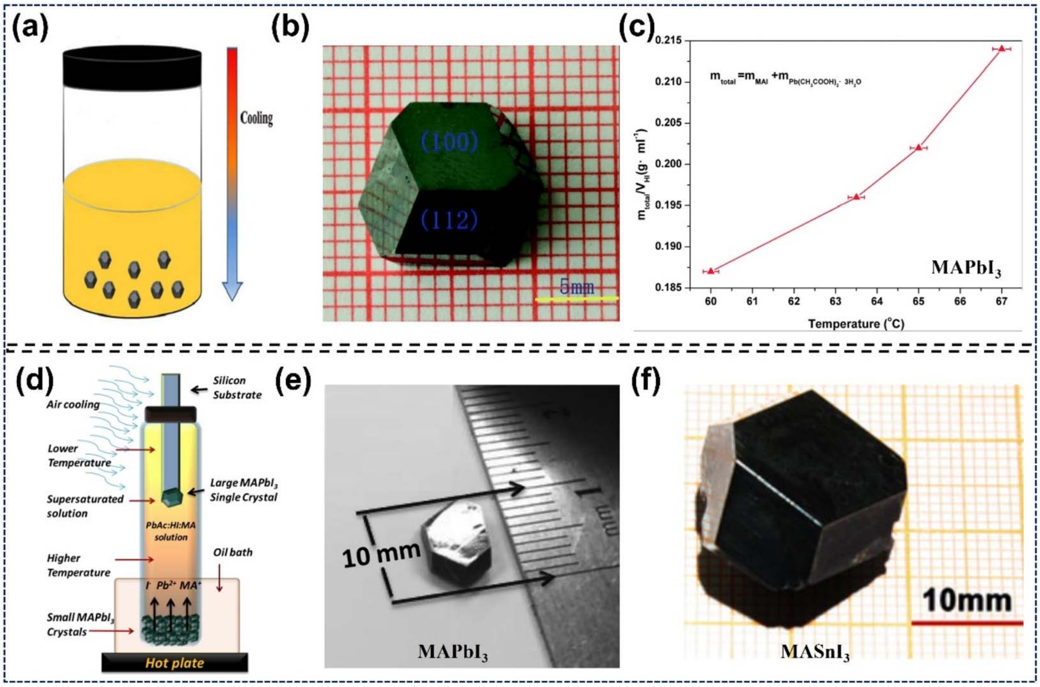

Fig. 8 The STL method to prepare single-crystal perovskite materials: (a and b) BSSG method and the images of single crystals obtained by this method.[76] Copyright 2015, Royal Society of Chemistry. (c) Solubility curve of $MAPbI_3$ in HI solution.[91] Copyright 2015, The American Association for the Advancement of Science. (d–f) Schematic illustration of the TSSG method and the single crystals prepared by this method.[120] Copyright 2016, Wiley-VCH.

3.1. Growth of bulk single crystals

3.1.1. Solution temperature lowering (STL) method. In 1987, Poglitsch and Weber pioneered the synthesis of $CH_3NH_3PbX_3$ (X = Cl, Br, I) perovskite crystals *via* controlled cooling of concentrated aqueous HX acid solutions from elevated temperatures (~100 °C) to ambient conditions.[118] However, this initial approach predominantly yielded small-sized crystals, necessitating subsequent methodological refinements to achieve larger crystal dimensions. The STL method, a refined adaptation of Weber's pioneering technique, is a classic method for fabricating large-sized single-crystal perovskite materials. This method operates on the principle that perovskite solubility diminishes progressively as the temperature of a hot saturated solution decreases, triggering crystal precipitation upon reaching supersaturation. Specifically, large-sized single-crystal perovskites can be obtained by gradually cooling a precursor solution containing preformed seed crystals until supersaturation. Depending on the different fixed positions of the seed crystal, the crystal growth techniques are divided into top-seeded solution growth (TSSG) and bottom-seeded solution growth (BSSG). As a typical example, Tao's group obtained $MAPbI_3$ single crystals with dimensions of 10 mm × 10 mm × 8 mm by using a BSSG method. The crystal growths were performed in a thermostatically controlled water bath using hydroiodic acid (HI) as the solvent, with the solution saturated at 65 °C. $MAPbI_3$ seed crystals were preheated to 70 °C for 24 h to ensure complete dissolution. Bulk single crystals of $MAPbI_3$ were grown over approximately one month by cooling the solution from 65 °C to 40 °C to induce saturation (Fig. 8a–c).[76] In the same year, Huang's group reported the successful growth of large-size $MAPbI_3$ single crystals (≈10 mm) *via* the TSSG method. The process involves three key steps: first, cooling the mixed solution to 75 °C and maintaining this temperature for one day to induce the precipitation of seed crystals; second, transferring these seed crystals to a container with a piece of silicon substrate; and finally, leveraging convective effects within the chamber to accelerate the nucleation of seed crystals on the silicon substrate, thereby facilitating the formation of large-sized crystals (Fig. 8d and e).[91] Subsequently, Lian *et al.* prepared centimeter-sized $MAPbI_3$ bulk single crystals using the BSSG method.[119] Yan *et al.* obtained bulk single crystals with dimensions of 20 mm × 18 mm × 6 mm *via* a rapid solution temperature-lowering method.[99] Recently, Tao's group synthesized bulk $MASnI_3$ and $FASnI_3$ single crystals through the TSSG method (Fig. 8f).[120] Additionally, Ma *et al.* fabricated carbon-based $CsPbI_2Br$ perovskite solar cells using the TSSG method, achieving a PCE exceeding 14% while significantly enhancing device stability. This method effectively reduces film defects and improves crystallization quality.[121]

3.1.2. Inverse temperature crystallization (ITC) method. Similar to the aforementioned STL method, ITC is also based on the abnormal solubility behavior of solutes across varying temperatures. The key distinction lies in that, within specific organic solvents, the solubility of these solutes exhibits a decreasing trend as the temperature rises. Bakr's group was the first to employ this method to synthesize a series of bulk $MAPbX_3$ (X = Cl, Br, I) and $FAPbX_3$ (X = Br, I) single crystals (Fig. 9a and b). Utilizing ITC, size/morphology-controlled crystals with low trap density and favorable charge transport properties can be rapidly obtained in hot solutions. It is worth noting that owing to different combinations of perovskite precursors and organic solvents, the crystals precipitate in some organic solutions, and not in others. For example, γ-butyrolactone (GBL) is a suitable solvent for forming $MAPbI_3$ crystals, while $MAPbBr_3$ crystals are suitable for being formed in *N*,*N*-

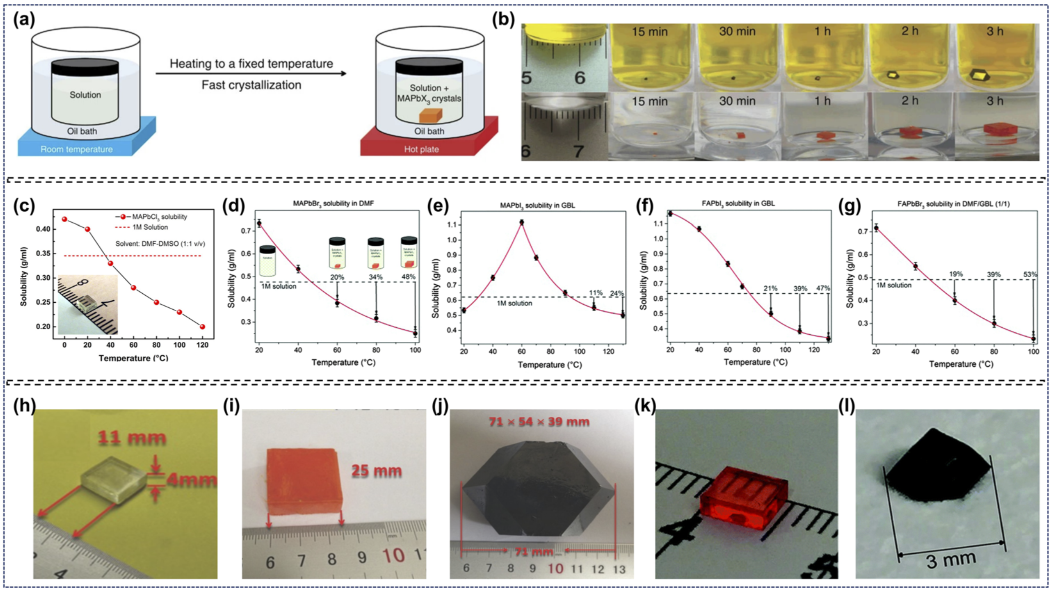

Fig. 9 Inverse temperature crystallization for single-crystal perovskites: (a and b) schematic illustration of the ITC method.[81] Copyright 2015, Springer Nature. (c–g) Temperature-dependent solubility of perovskite materials in certain organic solvents; (h–l) single crystals prepared by the ITC method.[103,104,122] Copyright 2015, American Chemical Society. Copyright 2015, Royal Society of Chemistry. Copyright 2015, Wiley-VCH.

dimethylformamide (DMF) solutions. In addition, researchers uncovered the role of surface tension in the rapid synthesis of single-crystal perovskites by using the ITC method during the process of investigating its nucleation and growth mechanisms (Fig. 9c–g).[81,122–124] Subsequently, Liu's group prepared inch scale crystals by using the combination of seed-induced and ITC method. First, a large number of ≈1–2 mm seed crystals were collected in the hot mixed solutions, which were kept at 100 °C for two days. Then, a larger crystal was obtained by placing the original seed in the precursor solution. Finally, inch scale single-crystal perovskites could be harvested by repeating the above growth step several times. It is worth noting that the speed of growth is related to the size of seed crystals (Fig. 9h–l).[103] Owing to the slow growth rate of traditional solution crystallization processes, Tao *et al.* prepared a centimeter-sized $MAPbI_3$ single crystal by utilizing N_2 air flow to increase solvent evaporation in the inverse temperature crystallization process.[125] To improve the optoelectronic properties of $FAPbBr_3$, Zhang *et al.* prepared Cl-doped $FAPbBr_3$ single-crystal perovskites using the ITC method. Among these, $FAPbBr_{2.9}Cl_{0.1}$ exhibited the longest carrier lifetime. Youn S. S. O *et al.* used the ITC method to prepare Bi-doped $MAPbBr_3$ to explore the effect of Bi concentration on the single crystal performance.[122]

3.1.3. Slow evaporation (SE) method. Compared with the STL and ITC methods, SE is a simpler and more convenient approach. It forms perovskite crystals *via* controlled solvent evaporation at a constant temperature (Fig. 10a).[126] In 1997, Jakubas *et al.* adopted SE to prepare $[NH_2(CH_3)_2]GaCl_4$ (DMACG) single crystals.[127] Liao *et al.* obtained bulk $(C_6H_5CH_2NH_3)_2PbCl_4$ single crystals with dimensions of 5 mm × 10 mm × 2 mm *via* slow evaporation. First, small crystals were synthesized from a concentrated aqueous HCl solution containing $PbCl_2$ and benzylammonium chloride in the required stoichiometric ratio. Then, large crystals were harvested by controlled evaporation of the DMF solution at 363 K (Fig. 10b).[128] For instance, Huang *et al.* prepared colorless $(C_6H_5C_2H_4NH_3)_2CdI_4$ crystals at room temperature *via* slow solvent evaporation of a mixed solution, containing menthol, CdI_2 and pre-synthesized $C_6H_5C_2H_4NH_3I$ (Fig. 10c).[129] The SE method, easy to operate but with unsatisfactory performance, is not optimal for preparing large-sized, high-quality single crystals.

3.1.4. Anti-solvent vapor-assisted crystallization (AVC) method. In contrast to the aforementioned methods, the AVC method is temperature-independent and solely relies on the selected solvent. This is primarily attributed to the solvent-dependent solubility variations of perovskites.[12,25–27] As reported, perovskites display high solubility in GBL, DMF, and DMSO, but poor solubility in anti-solvents such as methylene chloride (DCM), acetonitrile (CAN), and chlorobenzene (CB).[16,86] For instance, the groups of Cheng and Seok employed the AVC method to improve the flatness and uniformity of thin-film photovoltaics.[130,131] Similarly, Bakr's group successfully obtained high-quality $MAPbX_3$ (X = Br, I) single crystals using this method, in which an appropriate anti-solvent was slowly and evenly diffused into the precursor solution to reduce the solubility of the perovskite, ultimately leading to the formation of bulk crystals. The process involved two key steps: first, the precursor solution was prepared by mixing MAX and PbX_2 (X = Br, I) in DMF or GBA; second, the container containing the precursor solution and DCM or GBA solvent was sealed, allowing DCM or GBA vapor to diffuse slowly into the precursor solution. As the diffusion proceeded, the concentration of the perovskite increased gradually, leading to the precipitation of bulk crystals from the solution. Specifically, they synthesized $MAPbBr_3$ crystals using a 1 : 1 molar ratio of MABr and $PbBr_2$ (Fig. 10d).[86] However, Huang's group demonstrated that a 0.8 molar ratio of MABr to $PbBr_2$ is more favorable for growing high-quality $MAPbBr_3$ crystals, which arises from the significant solubility difference

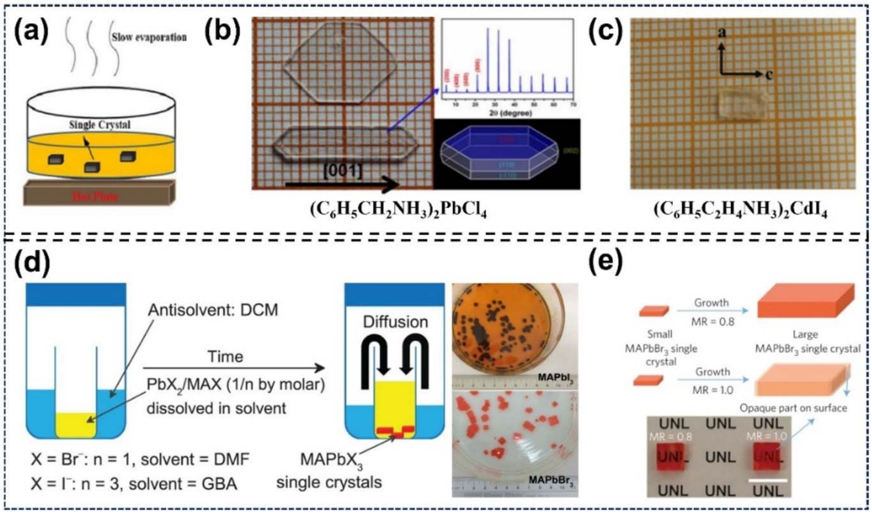

Fig. 10 SE and AVC methods for single-crystal perovskite preparation: (a–c) SE method schematics and resultant crystals.[128,129] Copyright 2015, Springer Nature. Copyright 2017, Royal Society of Chemistry. (d) AVC method schematics and harvested crystals.[86] Copyright 2015, The American Association for the Advancement of Science. (e) Photographs of $MAPbBr_3$ single crystals with different molar ratios.[16] Copyright 2016, Springer Nature.

between the two components (Fig. 10e).[16] Additionally, other perovskites including $CsPbBr_3$ and Cs_4PbBr_6 crystals were also synthesized successfully by the AVC method.[43,44]

3.2. Growth of thin single crystals

Bulk single-crystal perovskites grown in three dimensional spaces exhibit high light absorption loss due to their large thickness, rendering them unsuitable for direct application in vertical-type optoelectronic devices. However, this structure is actually superior to planar-type optoelectronic devices. Consequently, there is an urgent need for single-crystal perovskite wafers to develop high performance optoelectronic devices.[37,38,132,133]

3.2.1. Chemical vapor deposition method (CVD). While high quality single-crystal perovskites have been obtained *via* wet-chemical methods, the solvents, surfactants, and other unintended impurities introduced during the solution-phase synthesis process will compromise the purity and overall quality of the final materials. As a solvent-free fabrication technique, CVD demonstrates exceptional performance in regulating thin film morphology, minimizing surface defects, and improving material quality and stability. As shown in Fig. 11a, CVD growth

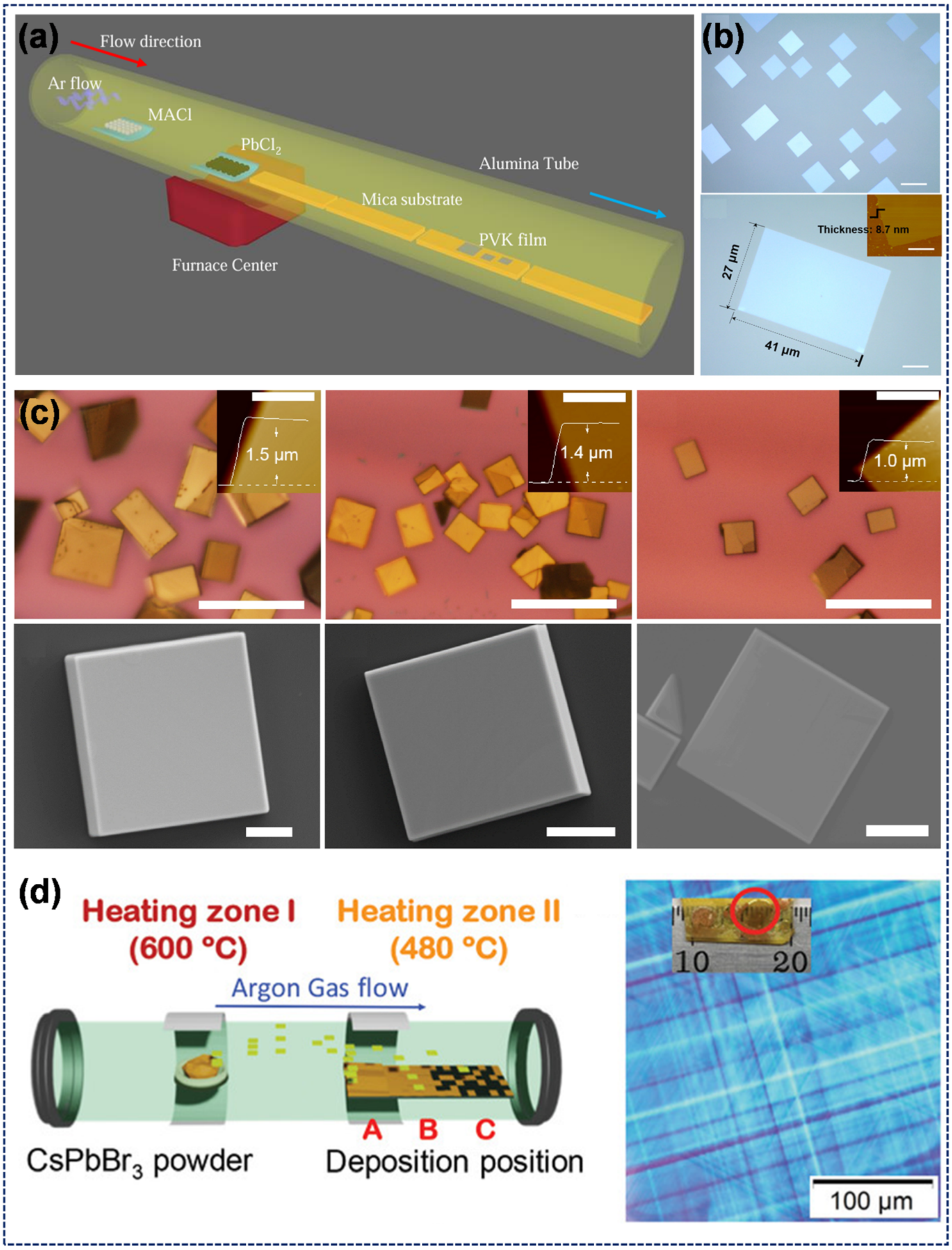

Fig. 11 CVD method for single-crystal perovskite preparation: (a and b) schematic illustration and film morphology of the CVD synthesis of $MAPbCl_3$.[134] Copyright 2015, Royal Society of Chemistry. (c) Photographs and AFM images of $CsPbX_3$ (X = Cl, Br, I) microplatelets.[135] Copyright 2017, Springer Nature. (d) Schematic of the CVD setup with variable substrate positions and corresponding image of $CsPbBr_3$ single crystal thin films prepared *via* the CVD method.[136] Copyright 2021, Wiley-VCH.

involves a tube with the carrier gas inlet on the left and a vacuum-pumped exhaust port on the right. The gas flow transports precursors to the substrate for sequential reactions, deposition and crystallization. Shi *et al.* adopted this configuration to obtain ultrathin (sub-10 nm) and large scale (a few tens of micrometers in lateral dimension) single crystalline 2D perovskite thin films on layered muscovite mica. Ordered perovskite films were successfully obtained, yet significant lattice mismatch and entirely disparate lattice types were observed between the substrate and the target material (Fig. 11b).[134] Duan *et al.* demonstrated the one-step CVD growth of $CsPbX_3$ (X = Cl, Br, I) microplatelets on diverse substrates (Si/SiO_2 wafers, reduced graphene oxide, graphene, and 2D MoS_2). All $CsPbX_3$ microplatelets show intense, tunable PL covering blue, green and red bands. Particularly, $CsPbBr_3$ microplatelets serve as dual gain media and WGM cavities to enable room-temperature lasing, while graphene/$CsPbBr_3$/graphene heterostructures can fabricate vertical photodetectors with high photocurrent gain (Fig. 11c).[135] In 2021, Nie *et al.* successfully fabricated high-quality and large-area $CsPbBr_3$ SCTFs with millimeter-scale crystalline grains. This was accomplished by systematically varying substrate types and positions to precisely control the deposition rate and growth temperature, resulting in a maximum lateral grain size exceeding 3.1 mm (Fig. 11d).[136] Although CVD is applicable for large-scale thin-film fabrication, both single-source ($CsPbBr_3$) and dual-source (CsBr, $PbBr_2$) deposition strategies for $CsPbBr_3$ present prominent challenges. For the former, unvalidated congruent evaporation causes Cs/Pb-enriched films with low phase purity. For the latter, surface kinetics disturb component concentrations, rendering it prone to forming impurity phases during $CsPbBr_3$ deposition. As per these considerations, Li *et al.* investigated single-/dual-source deposition for phase-pure $CsPbBr_3$. By analyzing evaporation products *via* Knudsen Effusion Mass Spectrometry and growth products at varied temperatures, they found that $CsPbBr_3$ decomposes partially congruently with precursor composition shifts; raising the temperature mitigates this by desorbing excess $PbBr_2$. Dual-source evaporation yields high-purity $CsPbBr_3$ at elevated temperatures (CsBr-limited

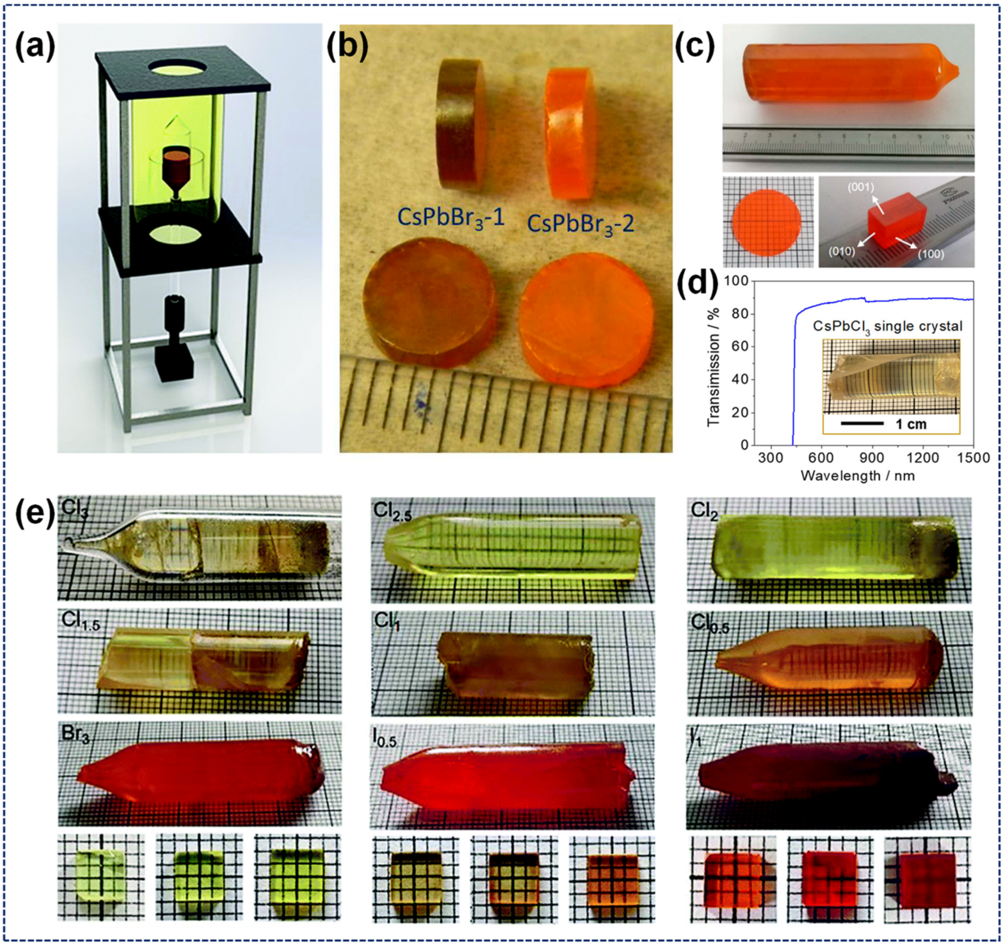

Fig. 12 Bridgman method for single-crystal perovskite preparation: (a) diagram of the homemade Bridgman furnace.[138] Copyright 2021, Royal Society of Chemistry. (b) Photograph of the single-crystal specimens of $CsPbBr_3$.[139] Copyright 2013, American Chemical Society. (c) Photographs of the as-grown $CsPbBr_3$ single crystal (upper), polished wafer (lower left), and oriented cuboid $CsPbBr_3$ single crystal (lower right).[140] Copyright 2018, American Chemical Society. (d) Optical transmission of $CsPbCl_3$ single crystals. Inset: Bridgman-grown $CsPbCl_3$ ingot.[141] Copyright 2021, American Chemical Society. (e) Photographs of the as-grown $CsPbBr_{3-3n}X_{3n}$ bulk crystals.[138] Copyright 2021, Royal Society of Chemistry.

growth), while lower temperatures lead to impurity phases ($CsPb_2Br_5$, Cs_4PbBr_6).[137]

3.2.2. Bridgman method. The Bridgman method, a conventional yet reliable crystal growth technique for melt-grown crystals, relies on precisely tailored temperature gradients and controlled solidification to produce large, high-quality crystals with negligible defect density. Fig. 12a is the three-dimensional diagram of a typical Bridgman furnace. Divided into four stages (raw material melting, gradient regulation, crystal growth, extraction and processing), the Bridgman growth process achieves high-quality single crystals by precise temperature control and slow crucible movement to establish stable gradients, enabling bottom-to-top crystallization followed by cooling, extraction, cutting and polishing.[138] Kanatzidis and co-workers pioneered $CsPbBr_3$ synthesis by the vertical Bridgman method, obtaining 7 mm diameter crystal ingots *via* a three-zone furnace at 10.0 mm h^{-1} translation speed under a set temperature profile, as shown in Fig. 12b.[139] As shown in Fig. 12c, Tao *et al.* prepared high-quality large-sized $CsPbBr_3$ single crystals *via* repeated directional crystallization and impurity removal, improving carrier transport properties. By means of the X-ray orientation technique, they carried out the first-ever exploration of the material's anisotropic optoelectronic properties, uncovering distinct variations in optoelectronic performance across various crystal planes. This threefold enhancement in responsivity and EQE of the optimal plane stems from the modulation of carrier transport enabled by the material's structural anisotropy.[140] Large-size $CsPbCl_3$ single crystals were synthesized *via* the Bridgman method, as illustrated in Fig. 12d. The resultant crystals are pale-yellow and feature high optical transparency, with transmittance exceeding 80% across a broad wavelength range. Such high optical transparency is indicative of low impurity content in the $CsPbCl_3$ single crystals.[141] Furthermore, Zhang *et al.* obtained

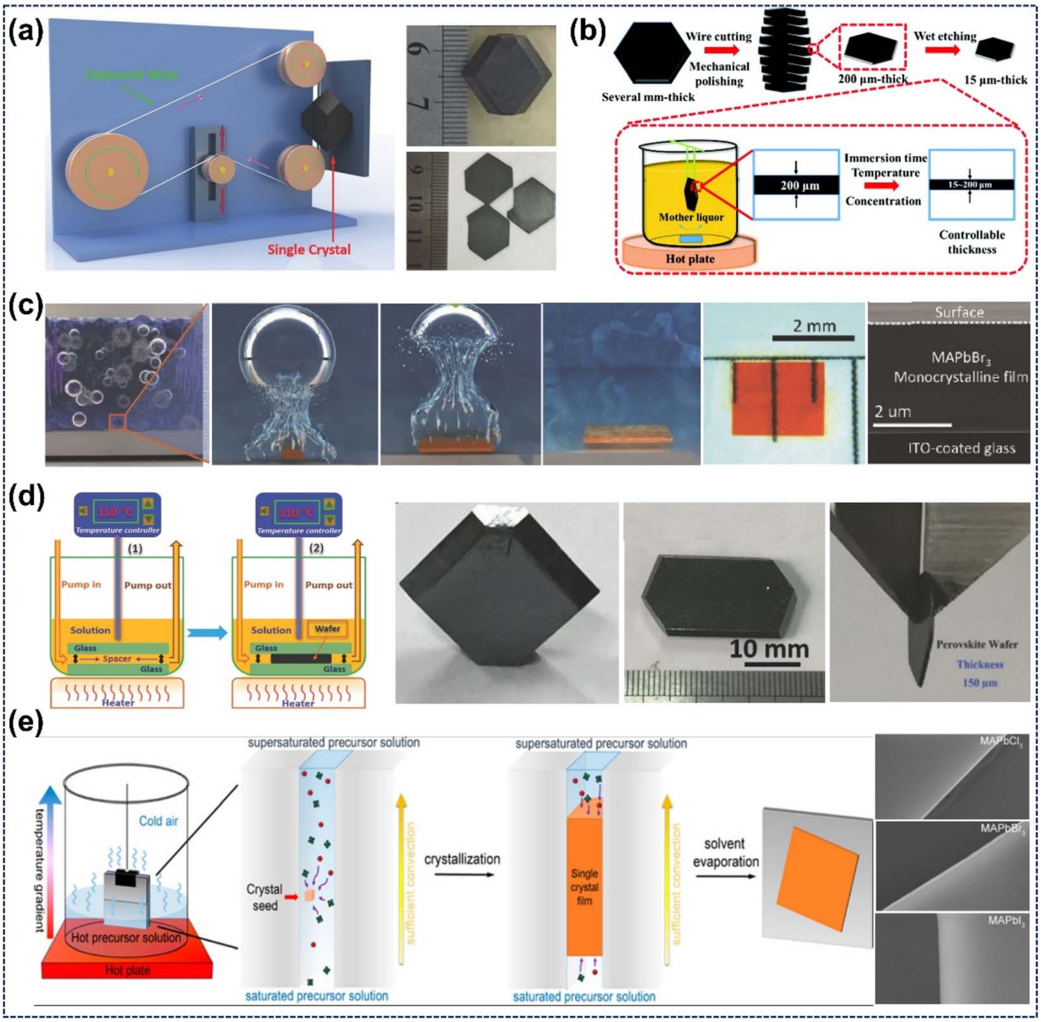

Fig. 13 Fabrication of single-crystal perovskite wafers and growth mechanism of their thin crystals: (a) schematic of diamond wire sawing machine and sliced $FAPbI_3$ wafers.[38] Copyright 2016, Wiley-VCH. (b) $MAPbI_3$ single-crystal film fabrication process.[47] Copyright 2018, Royal Society of Chemistry. (c) Microscopic CTAC mechanism schematic and resulting monocrystalline film.[82] Copyright 2016, Wiley-VCH. (d) Ultrathin single-crystal wafer preparation schematic and microreactor-grown wafers.[48] Copyright 2016, Wiley-VCH. (e) Space-limited technique schematic for on-substrate growth of large-area, thickness tunable single-crystalline perovskite thin films.[36] Copyright 2016, American Chemical Society.

centimeter-sized bulk single crystals of $CsPbBr_{3-3n}X_{3n}$ using a modified Bridgman technique. Specifically, polycrystalline precursors were first synthesized, followed by heating at a temperature ranging from 550 to 650 °C for 6 h in a home-made vertical furnace equipped with dual temperature zones. The precursors were then slowly transferred to the low-temperature zone to induce crystallization, after which the system was cooled to room temperature at a controlled rate of 5–15 °C h^{-1}. The as-grown crystals exhibited high structural stability and tunable optoelectronic properties, and were subsequently processed *via* cutting to obtain samples with dimensions of 7 mm × 7 mm × 1.5 mm (Fig. 12e).[138] Although the Bridgman method enables the production of large-size crystals in sealed ampoules, the interfaces between the crystal and the ampoule may induce internal stress, fissures or microscopic grain boundaries within the crystals. Moreover, it is only suitable for organic–inorganic compounds with established melting points, as organic substances exhibit high vapor pressure and poor chemical stability at melting temperatures.

3.2.3. Other types of growth methods for thin single-crystal materials. Currently, the growth technology of single-crystal perovskite wafers has become a research hotspot, as it is suitable for improving device performance. Liu's group sliced the as-prepared large $FAPbI_3$ crystals into thin wafers ($\approx$100 μm) using a diamond wire sawing machine. As shown in Fig. 13a, the large $FAPbI_3$ crystals were mounted on the sample holder of the slicing machine, and moved slowly toward the revolving wire at a specific speed. By controlling the sawing speed and crystal feeding rate, perovskite wafers with well-defined shapes and sizes could be obtained.[38] Subsequently, Bakr's group fabricated high-quality $MAPbBr_3$ single-crystal perovskites ($\approx$150 μm) *via* mechanical polishing.[142] Yan's group obtained $MAPbI_3$ perovskite single-crystal thin films ($\approx$15 μm) by treating the cut and polished samples using a chemical etching technique (Fig. 13b). The sliced and polished wafers ($\approx$200 μm thick) were immersed in an etching solution, which was the residual mother liquor from bulk crystal growth. By controlling the immersion time, etching solution concentration and temperature, the desired wafer thickness could be achieved.[47]

Apart from these methods, the cavitation-triggered asymmetrical crystallization (CTAC) method and space-limited technique have also gained favor among researchers. In 2016, Bakr's group obtained homogeneous $MAPbBr_3$ perovskite single-crystal thin films with thickness ranging from 1 to 60 μm using the CTAC method assisted by ultrasound. Fig. 13c illustrates the entire CTAC process. Owing to the successive cyclic compression and rarefaction of ultrasound waves, cavities are created and collapsed, releasing ultrahigh energy that can induce nucleation. This energy can typically overcome the nucleation barrier formed by rapid cooling in local zones, increased local pressure, and energy accumulation. Additionally, the growth of asymmetric crystals is related to the collapse of cavities, which is typically asymmetric near the solid surface, and their high-speed fluid can jet toward the substrate.[82] Liu's group successfully prepared a series of $\approx$150 μm thin wafers using the space-limited technique in a dynamic flow micro-reactor system (Fig. 13d). The gap between the two thin glass slides plays a crucial role in determining the thickness of the resulting samples.[48] Subsequently, the Kuang and Huang groups adopted a similar technique to grow thin perovskite single-crystalline wafers of approximately 10 μm.[35,84] Hu's group reported a facile space-confined solution-processed strategy to on-substrate grow various hybrid perovskite single-crystalline thin films in the size of submillimeter with adjustable thicknesses from nano- to micrometers. As illustrated in Fig. 13e, two clean flat substrates were clipped together and then vertically dipped in perovskite precursor solution. Capillary pressure enabled the solution to spread over the entire substrates, while the thickness of perovskite single-crystalline thin films was well-defined by the inter-substrate gap, which can be easily tuned by the clipping force.[36] Notably, Ma's group optimized the thickness of single-crystalline thin films down to hundreds of nanometers by improving the previous preparation method, which provides the possibility of obtaining large-area single-crystalline thin-films. Specifically, they improved the previously reported ITC technique in three aspects:

(1) Growing crystals between two face-to-face substrates with a micrometer-sized gap to disrupt isotropic growth.

(2) Controlling thickness *via* pressure applied to the gap.

(3) Conducting surface modification on substrates (hydrophobic treatment of silicon surface and oxygen plasma treatment of ITO surface).[143]

3.3. Growth of single crystal nanostructures

Owing to their size-dependent and excellent optoelectronic properties, single-crystalline perovskite nanostructures show exceptional promise for application in nanoscale optoelectronic and photonic devices, particularly in the realization of miniaturized lasers.[39,42] Since the preparation methods of these materials play a vital role in improving device quality, numerous researchers have focused on the controlled synthesis of perovskite single-crystalline nanostructures.[34,41,50] For example, Jin's group obtained single-crystalline $CH_3NH_3PbX_3$ (X = Cl, Br, I) nanowires with a length of approximately 20 μm and flat rectangular end facets *via* a surface-initiated solution growth strategy. These nanowires were synthesized by immersing a $Pb(CH_3COO)_2$ thin film (deposited on a glass slide) in an isopropanol solution of MAX under ambient conditions at room temperature. They also observed room temperature lasing operations in most NWs with mixed stoichiometries, covering the emission range from the near-infrared to the visible region (Fig. 14a and b).[15] Subsequently, they adopted the same method to harvest single-crystalline $FAPbX_3$ (X = Br, I) nanowires, which exhibit better photostability and wider wavelength tunability than MA-based counterparts. Among them, both $FAPbI_3$ and $FAPbBr_3$ NWs demonstrated lasing behavior with low lasing thresholds (several microjoules per square centimeter) and high quality factors (1500–2300. In particular, $FAPbI_3$ (and MABr-stabilized $FAPbI_3$) NWs exhibited optically pumped room temperature near-infrared (~820 nm) lasing, whereas $FAPbBr_3$ showed green lasing. They further demonstrated tunable nanowire lasers operating across a broader wavelength range, which are based on FA-based lead halide perovskite alloys (FA,

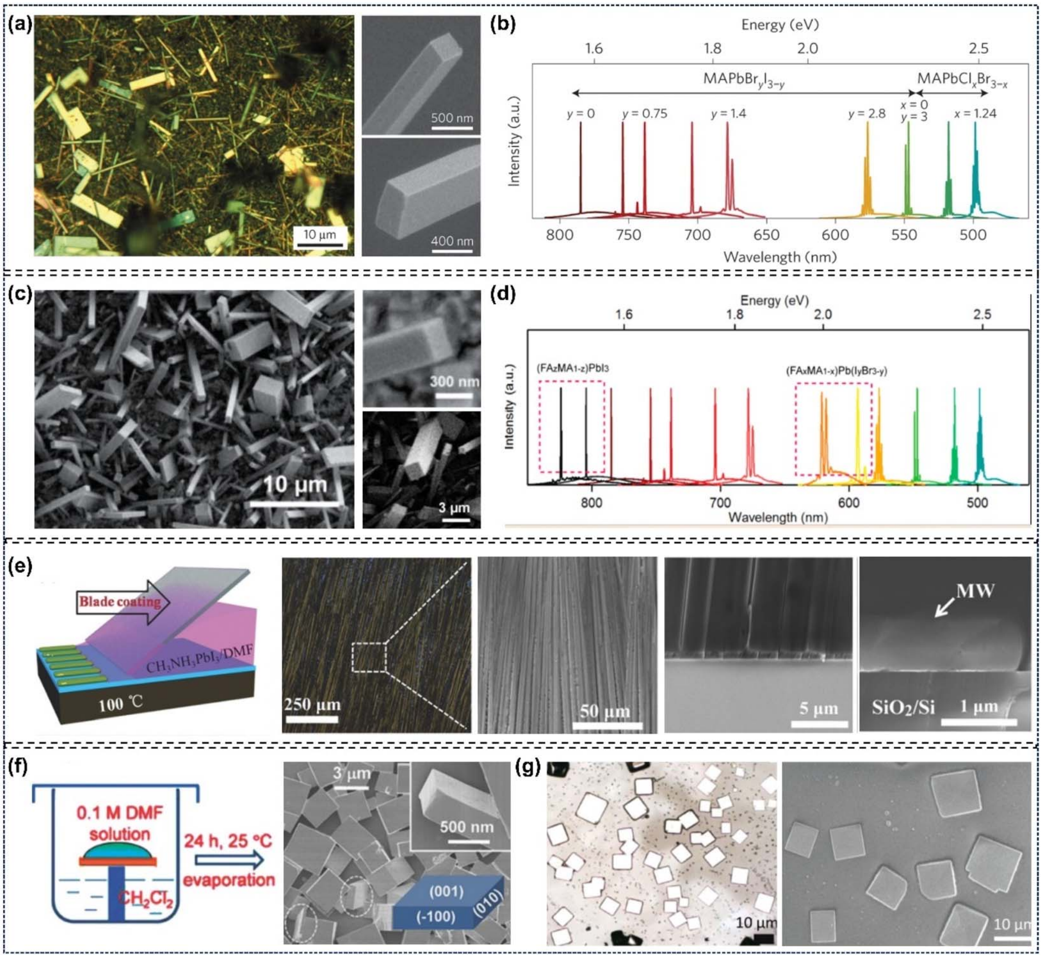

Fig. 14 The structural characterization of single-crystal perovskite nanostructures: (a) optical and magnified SEM images (top view) of single crystal $MAPbI_3$ perovskite nanowires; (b) widely tunable lasing emission wavelengths at room temperature from single-crystal NW lasers of mixed lead halide perovskites.[15] Copyright 2015, Springer Nature. (c) SEM images of as-grown MABr-stabilized $FAPbI_3$ perovskite nanowires; (d) broad wavelength-tunable lasing from $FA_{0.67}MA_{0.33}PbBr_{2.69}I_{0.31}$ NWs.[17] Copyright 2016, American Chemical Society. (e) Schematic illustration, optical images, and SEM images of $MAPbI_3$ microwire arrays.[144] Copyright 2016, Wiley-VCH. (f) Low-magnification and high-magnification SEM images of single-crystalline square $MAPbBr_3$ perovskite microdisks.[146] Copyright 2015, Wiley-VCH. (g) Optical microscopic images and top-view SEM image of single-crystalline $CH_3NH_3PbBr_3$ microplatelets.[148] Copyright 2019, Wiley-VCH.

MA) PbI_3 and (FA, MA) Pb (I, Br)$_3$ *via* cation and anion substitutions (Fig. 14c and d).[17] Subsequently, Jie's group reported dragging a DMF solution of $MAPbI_3$ across a hot (100 °C) substrate. After evaporation of the exposed solution front, $MAPbI_3$ microwire arrays formed, which are primarily aligned along the blade movement direction and have lengths of up to 1 cm. The scanning electron microscopy images revealed that the as-synthesized samples were straight with uniform width ranging from 2 to 3 μm. The molecular layers feature a smooth top surface and homogeneous color variation across the entire region, indicating the single-crystal nature of the perovskite molecular layers. Further characterization of the smooth cross-sectional surface of the molecular layers also confirms their high crystallinity (Fig. 14e).[144] Meanwhile, Zhu's group prepared patterned $MAPbBr_3$ single-crystalline microplates on an FTO substrate *via* an Ostwald ripening assisted photolithography (ORAP) method.[145] Fu's group obtained single-crystalline square $MAPbBr_3$ microdisks with a thickness of approximately 500 nm through a one-step solution self-assembly process (Fig. 14f).[146] Additionally, Xiong's group synthesized single-crystalline $CH_3NH_3PbX_3$ (X = Br, I) and $CH_3NH_3PbI_xCl_{3-x}$ nanowires using a two-step vapor phase method. First, PbX_2 (X = Br, I) nanowires were prepared *via* the chemical vapor deposition (CVD) method in a quartz tube. Then, the target products were formed through gas–solid heterophase reactions between MAX molecules and PbX_2 nanowires using the same CVD method.[147] Wang's group achieved size-controlled single-crystalline $CH_3NH_3PbBr_3$ microplatelets and microstrips by adjusting the concentration of the precursor solution, *via* a process involving slow diffusion and evaporation of DMF (Fig. 14g).[148] Besides the widely studied single-crystalline organic lead halide perovskite nanostructures, some inorganic counterparts such as $CsPbBr_3$ have also been successfully synthesized.[23,33] Table 2 summarizes the merits, limitations, application ranges, and specific effects on material performance of the various growth methods.

Table 2 Systematic comparative evaluation of various growth methods

Growth method	Advantages	Disadvantages	Application scope	Impact on material performance
STL	Convenient operation; low cost	Materials/time consuming; nucleation control difficulty	Lab-scale small-batch basic research	High photoelectric conversion efficiency; stability restricted by interface defects
ITC	Fast growth rate; simple operation	Temperature sensitive; solvent limitation	Preparation of single-crystal samples for preliminary performance testing	High carrier mobility
SE	Low cost; simple equipment	Long growth cycle; small crystal size; high defect density	Lab-scale small-batch basic research	Medium carrier mobility; moderate stability
AVC	Fast growth rate; energy saving	Small crystal size; random growth	Rapid preparation of single-crystal samples for preliminary performance testing	High photoelectric conversion efficiency
Space-confined method	Controllable thickness	Small area; thickness control confined to the range of micrometer to tens of micrometers	Suitable for growth of single-crystal films	High interface defects
CVD	Low cost; defect reduction; high reproducibility	Precise parameter control required; temperature limitation	Suitable for industrial production	Consistent crystal orientation, significant carrier transport anisotropy
Bridgman method	Temperature tunable; high quality; large crystal size	Unsuitable for organic component growth	Preparation of high-purity bulk single-crystals for basic physical property research	Good crystal integrity, few deep-level defects, excellent stability

4. Applications

By virtue of their excellent semiconductor performance, perovskite ABX_3 materials have garnered substantial attention in diverse optoelectronic applications, including photodetectors, solar cells, light-emitting diodes, lasers, high-energy ray detectors and other fields.[24] In this section, we focus on summarizing several representative applications.

4.1. Photodetectors

Photoelectric conversion technology is pivotal in key application areas such as optical communication, environmental monitoring, and digital-image sensing. As devices that convert optical signals into electrical ones, photodetectors stand as ideal candidates for the optoelectronic field.[18] Studies indicate that single-crystal perovskite photodetectors exhibit superior stability and photoelectric performance compared to their polycrystalline counterparts.[48,119,122,149] Typically, the key parameters characterizing photodetector performance include responsivity (R), detectivity (D^*), external quantum efficiency (EQE), and response time (τ). Table 3 summarizes the key performance parameters for single-crystal perovskite photodetectors.

R is the ratio of photocurrent to incident light intensity, reflecting the efficiency of converting light into photocurrent, and can be calculated as follows:[43]

$$R = \frac{I_{\mathrm{ph}} - I_{\mathrm{dark}}}{PS} \tag{4}$$

where S denotes the effective illuminated area, P is the irradiance power density, and ΔI is the current difference under illuminated (I_{ph}) *versus* dark (I_{dark}) conditions. Given that a higher D^* value implies superior weak signal detection capability, this parameter serves as a critical metric for evaluating photodetector sensitivity and can be expressed as:[20,45]

$$D^* = \frac{R\sqrt{S}}{\sqrt{2eI_{\mathrm{dark}}}} \tag{5}$$

where e is the elementary charge. EQE is an important parameter used to quantify the efficiency of photon to photocurrent conversion and can be determined as follows:[14,95]

$$\mathrm{EQE} = R\frac{hc}{\lambda e} \tag{6}$$

where h is Planck's constant, c is the speed of light, and λ is the wavelength of incident light. Parameter τ, the photoelectric conversion transit time of the photodetector, characterizes temporal response latency: the output electrical signal shows finite rise time to steady state under illumination and delayed decay when irradiation stops. Specifically, τ is defined as the duration required for the photoresponse to rise from 10% to 90% of its initial value or fall from 90% to 10% of its maximum value.[28,37]

As early as 2015, Lian *et al.* fabricated a high performance planar-type $MAPbI_3$ single-crystal photodetector (MSCP) by depositing a pair of interdigitated Au-film electrodes on the $MAPbI_3$ (100) facet (Fig. 15a). Under uniform illumination at 1 mW cm^{-2} irradiance, the MSCP exhibited an R value of 2.55 A W^{-1} and an EQE value of 5.95×10^2%, while the $MAPbI_3$

Table 3 Summary of detection performances of perovskite single-crystal photodetectors

Sample	Responsivity [A W^{-1}]	Detectivity [Jones]	EQE [%]	Rise time [10–90%]	Decay time [90–10%]	Ref.
$MAPbCl_3$	0.046	1.2×10^{10}	—	24 ms	62 ms	122
$MAPbCl_3$	3.73	9.97×10^{11}	1115	130 ns	368 μs	87
$MAPbBr_3$	0.115	—	3.17	2.3 s	2.76 s	150
$MAPbBr_3$	55.7	8×10^{13}	13 453	27.6 μs	15.8 μs	46
$MAPbBr_3$	4×10^3	—	1.5×10^4	—	25 μs	95
$MAPbBr_3$	1.6×10^7	1.3×10^{13}	1.5×10^7	81 μs	892 μs	143
$MAPbBr_3$	0.043	5.29×10^{10}	—	453 μs	493 μs	201
$MAPbBr_3$	7	4.2×10^{11}	—	0.5 ms	0.78 ms	187
$MAPbI_3$	0.035	—	100	139 μs	227 μs	47
$MAPbI_3$	4.95	2×10^{13}	—	<0.1 ms	—	19
$MAPb(Br_xI_{1-x})_3$ ($x = 0.78$)	2.36	2.01×10^{12}	639	3.4 ms	3.6 ms	101
$FAPbI_3$	4.5	—	900	8.3 ms	7.5 ms	38
$(PEA)_2Pb(I_{1-x}Br_x)_4$	4.8	6.5×10^{13}	—	—	—	198
$CsPbCl_3$	32.8	4.22×10^{12}	10 867	200 μs	420 μs	199
$FAPbBr_{2.5}I_{0.5}$	0.059	4.95×10^{10}	34.51	202 μs	331 μs	200
$(FASnI_3)_{0.1}(MAPbI_3)_{0.9}$	0.53	7.09×10^{10}	82.5	22.78 μs	20.35 μs	8

polycrystalline film photodetector (MPFP) showed significantly lower values of 0.0197 A W^{-1} and 4.59%, respectively. These results confirm that the MSCP achieves over two orders of magnitude enhancement in both *R* and EQE compared to the MPFP (Fig. 15b and c). Transient photocurrent response measurements showed that the MSCP has a rise time of 74 μs after triggering and a decay time of 58 μs after irradiation is terminated. Its response speed is three orders of magnitude faster than that of the MPFP (Fig. 15d).[119] Subsequently, Ma's group fabricated an $MAPbBr_3$ single-crystalline thin film (SCTF) photodetector with a thickness of 380 nm, and observed that optimizing the SCTF thickness could enhance both the lowest detectable power and internal gain by several orders of magnitude.[143] Liu's group reported that they prepared approximately 100 photodetectors on a piece of $MAPbI_3$ perovskite single-crystalline wafer, with the devices exhibiting a photocurrent about 350 times higher than that of comparable microcrystalline thin-film photodetectors (Fig. 15e–g).[48] They also developed a Vis-NIR photodetector based on dual-halide single-crystal perovskites, identifying the optimal response spectra at a bromine content of 0.78.[101] Additionally, Bakr's group exploited a photodetector based on $MAPbCl_3$ single-crystal perovskites, which is applicable for ultraviolet detection.[122] The single-crystal perovskite-based photodetectors fabricated by Huang's group realized a highly narrowband response with a full-width at half-maximum of <20 nm, attributed to the fast surface-charge recombination (Fig. 15h–j).[100] Meanwhile, Lin *et al.* fabricated photodetectors based on $MAPbBr_3/MAPbI_3$ single-crystalline photodiodes and photoresistors, which enabled photoresponses to near infrared light through trap-related linear sub-gap absorption.[29] Recently, Chang *et al.* employed low-temperature space-limited crystallization technology to prepare high-quality $(FASnI_3)_{0.1}(MAPbI_3)_{0.9}$ narrow-bandgap Sn–Pb mixed single-crystal perovskites, which were applied in high-performance near infrared photodetectors. The devices achieved an EQE of 82.5% with a response time of only 22.78 μs (Fig. 15k–m).[8] Yadav *et al.* investigated facet-dependent photodetection in $MAPbI_3$ single crystals, reporting ON/OFF ratios of ∼620 for the (112) facet and ∼410 for the (100) at a bias voltage of 10 V.[10]

At present, the majority of reported perovskite-based photodetectors are photoconductive types, which necessitate an external bias voltage for operation. Consequently, photovoltaic photodetectors have recently emerged as a promising alternative in the field, owing to their self-powered photodetector systems.[13,142,149] As a typical example, the Yan group designed a self-powered photodetector based on perovskite $MAPbI_3$ single crystals. The device operates *via* a built-in electric field generated by the Schottky junction between the Au and Al electrodes. It realized broadband detection across the wavelength range of 375 nm to 808 nm and demonstrates a responsivity of 0.24 AW^{-1} under an incident power density of 1×10^{-8} W cm^{-2} at 808 nm (Fig. 15n–p).[149] Meanwhile, Huang's group designed an X-ray detector with a typical p–i–p structure, which is based on the perovskite $MAPbBr_3$ single crystal.[16] The Wei group constructed a self-power photodetector based on a perovskite $MaPbBr_3/MAPbI_xBr_{3-x}$ heterojunction single crystal. This device is driven by the built-in electric field within the junction and exhibits a responsivity of 11.5 mA W^{-1} at 450 nm under zero bias, which is an order of magnitude higher than that of its pure $MAPbBr_3$ counterpart.[150] In 2025, Xu *et al.* developed self-powered perovskite quantum dot photodetectors *via* Cr^{3+} doping and MXene interfacial engineering. These devices exhibit a high responsivity of 186.9 mA W^{-1} and a detectivity of 1.85×10^{12} cm Hz$^{1/2}$ W^{-1}, showing strong potential for chlorophyll-*a* concentration monitoring based on the Beer–Lambert law. This study provides a novel approach for developing high-performance self-powered photodetectors and advancing water pollution monitoring.[9]

4.2. Solar cells

In recent years, PSCs have made remarkable strides in terms of PCE. This impressive progress is primarily attributed to the exceptional properties of semiconductor perovskite materials,

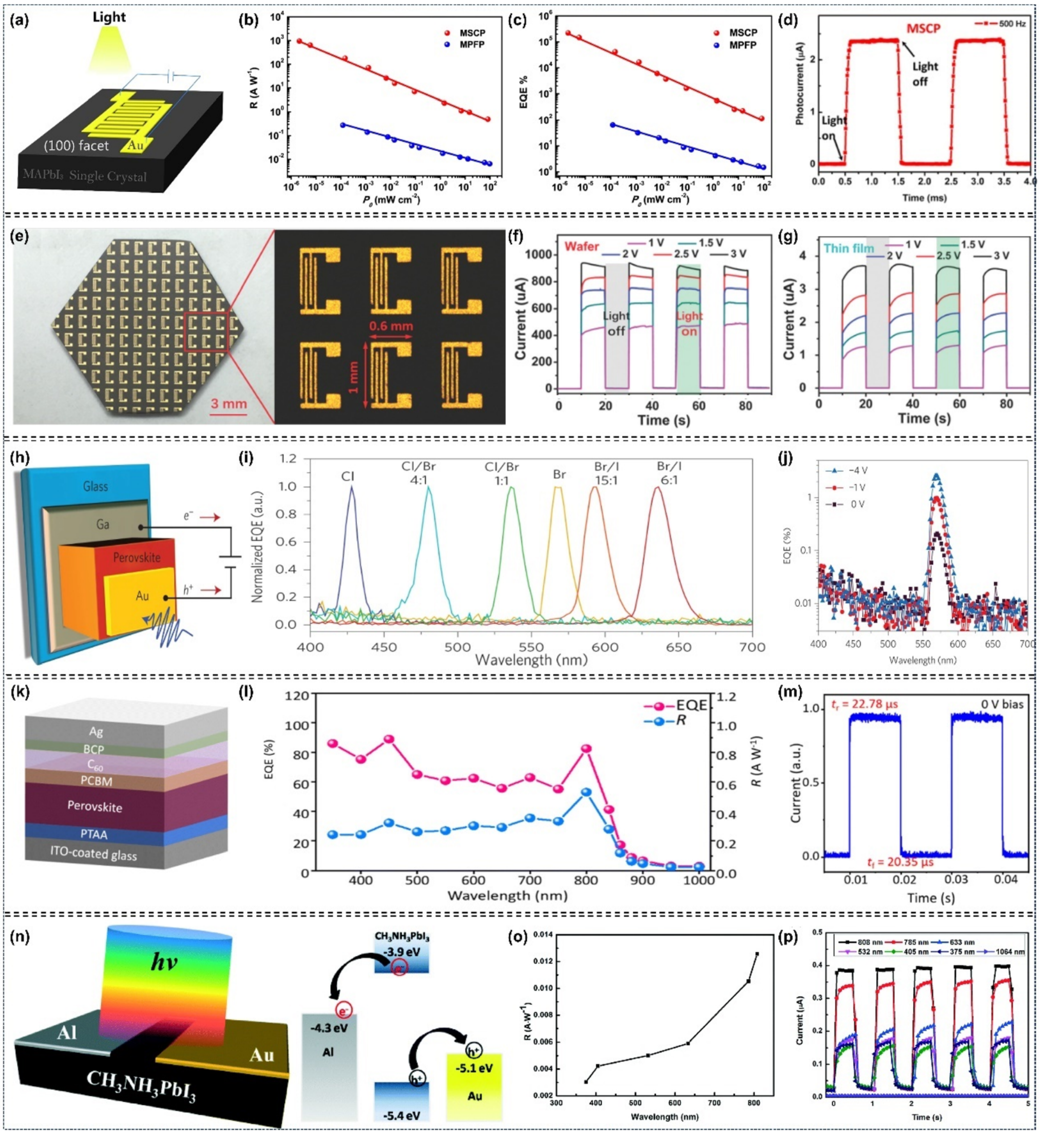

Fig. 15 Device structures and key performance parameters of single-crystalline perovskite photodetectors: (a–c) a planar-type $MAPbI_3$ single crystal photodetector, along with a comparison of responsivity and EQE between the as-fabricated MSCP and MPFP; (d) transient photocurrent response of the MSCP.[119] Copyright 2015, Springer Nature. (e–g) Photograph of approximately 100 photodetectors fabricated on an SC wafer, and a comparison of photocurrent response between the SC perovskite wafer and its SC thin film.[48] Copyright 2016, Wiley-VCH. (h–j) Device structure for realizing highly narrowband response and ultra-narrow tunable EQE spectra.[100] Copyright 2015, Springer Nature. (k–m) Structure and performance of multiple-layer device architecture with $(FASnI_3)_{0.1}(MAPbI_3)_{0.9}$ single crystal as the light absorption layer.[8] Copyright 2016, Royal Society of Chemistry. (n–p) A single-crystalline perovskite-based photovoltaic photodetector and its photoresponse characteristics at different irradiance wavelengths.[149] Copyright 2016, Royal Society of Chemistry.

which include high carrier mobilities, high optical absorption coefficients, long carrier diffusion lengths, and suitable band gaps for photovoltaic devices.[40,51,52,151] However, two significant challenges continue to impede the commercialization of PSCs: hysteresis effects and environmental instability. Hysteresis results in inconsistent performance under varying scanning conditions (forward and reverse scans), while environmental instability renders the cells vulnerable to degradation upon exposure to moisture, heat, or light. To address these issues, a growing body of research is now focusing on the development of single-crystal perovskite solar cells. The rationale behind this shift lies in the fact that single-crystal perovskites not only offer an ideal platform for deeper investigation into the operational principles of perovskite materials, but also facilitate the enhancement of PSC performance.[49,92,152] A prime illustration of this approach is the work carried out by the Bakr group. Leveraging the CTAC method supplemented by ultrasonic assistance, they successfully synthesized perovskite $MAPbBr_3$ single-crystalline thin films of 1–60 μm thickness. Subsequently, they fabricated straightforward PSCs with a configuration of the $FTO/TiO_2/MAPbBr_3(1\ \mu m)/Au$. Remarkably, the photovoltaic performance metrics of this single-crystal device were on par with those of its polycrystalline $MAPbBr_3$ counterparts. Specifically, it achieved a PCE of 6.53%, an open circuit

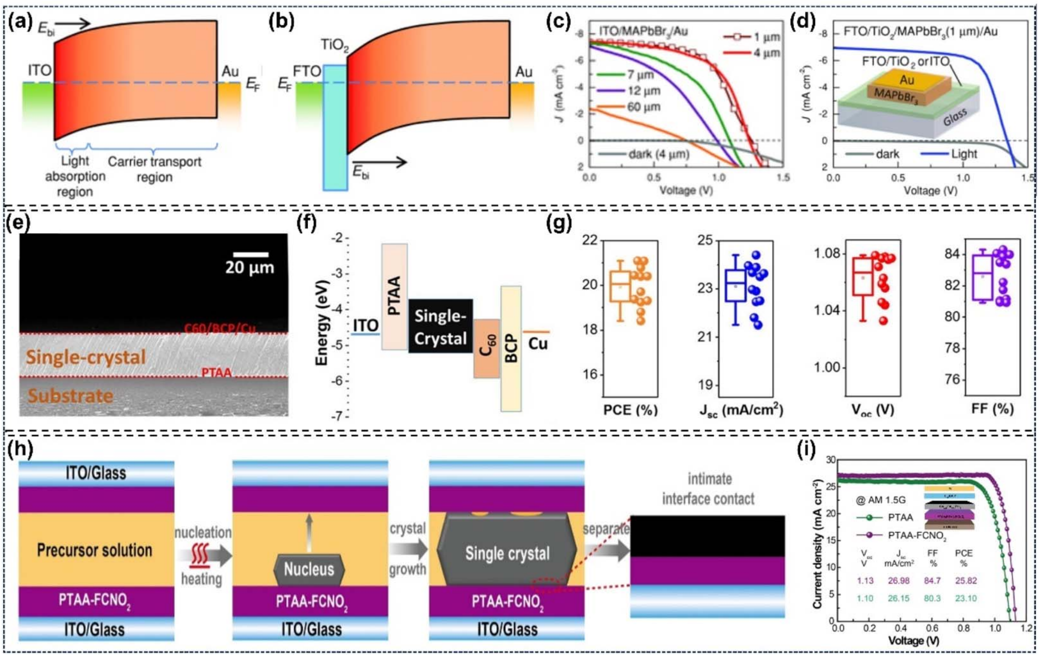

Fig. 16 Configuration and performances of single-crystalline perovskite-based solar cells: (a and b) band alignment diagrams for ITO/MAPbBr$_3$/Au and FTO/TiO$_2$/MAPbBr$_3$/Au configurations; (c and d) dark and illuminated *J*–*V* curves of ITO-based and FTO/TiO$_2$-based monocrystalline solar cells.[82] Copyright 2016, Wiley-VCH. (e and f) Cross-sectional SEM image and band alignment of a single-crystalline MAPbI$_3$ based solar cells; (g) statistical analysis of photovoltaic parameters of single-crystalline PSCs based on 12 devices.[152] Copyright 2019, American Chemical Society. (h) Schematic illustration of crystal nucleation and growth in confined spaces *via in situ* growth with PTAA-FCNO$_2$ HTLs; (i) *J*–*V* curves of single-crystal PSCs under AM1.5 light illumination (inset shows the device architecture).[7] Copyright 2025, Wiley-VCH.

voltage (V_{OC}) of 1.36 V, a short circuit current density (FF) of 6.96 mA cm^{-2}, and a fill factor (FF) of 0.69. These results underscore the potential of single-crystal perovskites to not only advance our fundamental understanding of perovskite materials but also to deliver competitive photovoltaic performance (Fig. 16a–d).[82] Furthermore, the Huang group successfully constructed lateral structured solar cells utilizing single-crystal perovskites, with the device architecture featuring Au/MAPbI$_3$/Au. Notably, for this particular lateral-structure, the device exhibited a remarkably high J_{SC} of 2.28 mA cm^{-2}, approximately 33 times higher than that of its polycrystalline counterpart, while the PCE of 1.88% at room temperature is 44-fold higher than that of the polycrystalline device.[77] Meanwhile, Zhou's research team fabricated an inverted solar cell based on $(FAPbI_3)_{0.85}(MAPbBr_3)_{0.15}$ single crystals. They conducted a systematic investigation into the key factors influencing device efficiency, ultimately obtaining a PCE of 12.18% under optimized conditions.[52] Subsequently, Bakr's research team adopted an ITC method, complemented by a space-limited approach, to successfully fabricate MAPbI$_3$ single-crystal thin films. They then designed a highly efficient single-crystal perovskite solar cell with the device architecture comprising ITO/PTAA/MAPbI$_3$ (20 μm)/C$_{60}$/BCP/Cu. This innovative design achieved an outstanding PCE of 21.09%, coupled with a FF of 0.835 (Fig. 16e–g).[152] Recently, Cheng and his research team have devised a strategy to regulate the nucleation process at the substrate surface by incorporating an additive into the hole transport layer, thereby effectively tackling the interface contact problem in single-crystal PSCs. This innovative approach not only establishes intimate interface contact and robust interlayer interaction but also optimizes the balance between electron and hole carrier extraction, while simultaneously suppressing interface nonradiative recombination. Consequently, they have achieved a remarkable PCE of 25.8%, representing the highest efficiency reported thus far for single-crystal PSCs. Additionally, the interface contact exhibits exceptional stability under thermal aging conditions, substantially enhancing the thermal durability of these single-crystal PSCs (Fig. 16h and i).[7] Table 4 provides a concise summary of the photovoltaic performance parameters for single-crystal PSCs. Additionally, we have compared the development trends of polycrystalline thin film-based and single-crystal thin film-based perovskite solar cells over the past five years. As shown in Fig. 17, perovskite solar cells based on single-crystal thin films have shown enormous development potential.

4.3. High-energy ray detectors

As ideal light-absorbing materials, single-crystal perovskites not only exhibit exceptional performance in photodetectors and solar cells but also show significant promise in high-energy ray detection, with applications spanning computed tomography, medical diagnostics, industrial nondestructive testing, and security screening systems. Their superior performance arises from three key advantages.

4.3.1. Large absorption coefficient. The integration of high atomic number elements (*e.g.*, Pb, I, Br) in single-crystal

Table 4 Summary of photovoltaic parameters of perovskite single-crystal solar cells

Device structure	J_{SC} [mA cm^{-2}]	V_{OC} [V]	FF	PCE [%]	Ref.
ITO/PEDOT:PSS/$MAPbI_3$ arrays/PCBM/ZnO/Al	8.69	0.52	0.379	1.73	51
ITO/PEDOT:PSS/$MAPbI_3$/PCBM/Ag	22.15	0.75	0.270	4.40	69
FTO/Cu/Au/Ag/LiF/PCBM//$MAPbI_3$/Spiro-MeOTAD/ITO/Au	≈13.5	1.15	≈0.296	≈4.50	92
Au/$MAPbI_3$/Au	2.28	0.82	≈0.710	5.36	77
FTO/TiO_2/$MAPbBr_3$/Au	6.96	1.36	0.690	6.53	82
FTO/TiO_2/$MAPbI_3$/Spiro-MeOTAD/Ag	22.28	0.66	0.590	8.78	49
ITO/NiO_X/$(FAPbI_3)_{0.85}(MAPbBr_3)_{0.15}$/$TiO_2$/Ag	23.14	1.03	0.510	12.18	52
ITO/Cu:NiO_X/$(TEA)_2(MA)_2Pb_3I_{10}$/PCBM/Ag	15.85	1.23	0.753	14.68	53
ITO/PTAA/$MAPbI_3$/PCBM/C_{60}/BCP/Cu	21.00	1.08	0.786	17.80	84
ITO/PTAA/$MAPbI_3$/C_{60}/BCP/Cu	23.46	1.07	0.835	21.09	152
ITO/MeO-2PACz SAM/$FA_{0.6}MA_{0.4}PbI_3$/C_{60}/BCP/Cu	27.50	1.07	0.770	23.10	167
ITO/SAM/PTAASAM/$MAPbI_3$/C_{60}/BCP/Cu	25.41	1.143	0.831	24.12	202
ITO/MeO-2PACz/$Cs_{0.05}FA_{0.95}PbI_3$/C_{60}/BCP/Cu	28.07	1.091	0.793	24.29	203
ITO/HTL/$Cs_{0.05}FA_{0.95}PbI_3$/C_{60}/BCP/Cu	26.15	1.10	0.803	25.80	7

perovskites endows them with strong absorption capabilities for high-energy photons (X-rays, γ-rays). This is attributed to the dependence of the X-ray attenuation coefficient αon atomic number Z of the material, following the relationship $\alpha \propto Z^4/E^3$, where E is the X-ray photo energy. Additionally, their linear attenuation coefficients are comparable to those of traditional scintillators such as CsI:Tl.[153]

4.3.2. Superior optoelectronic performance. The intrinsic low defect density of the single-crystal structure endows these materials with near-unity photoluminescence quantum yields, low trap densities, high charge carrier mobility, short fluorescence decay times (sub-nanoseconds to nanoseconds), and outstanding light yields (surpassing 30 000 photons per MeV in certain cases). These properties enable them to meet the rigorous requirements for rapid response and high sensitivity in high energy ray detection.[154–156]

4.3.3. Simple solution processability and bandgap tunability. Single-crystal perovskites can be synthesized through low temperature solution-based methods and exhibit tunable bandgaps. This allows optimization for specific detection wavelengths and facilitates their integration into flexible or large area devices.[157–159]

As early as 2016, Huang's group pioneered an $MAPbBr_3$ single-crystal-based X-ray detector, which showed approximately 33–42% and 16.4% detection efficiency for UV-vis light and X-ray photons, respectively. As shown in Fig. 18a–d, the device adopts a typical p–i–p configuration structure, with charge generation induced by both light and X-ray excitation. Notably, its sensitivity reached 80 μC Gy_{air}^{-1} cm^{-2}, surpassing commercial detectors by significant margins: 10 times that of the Cd(Zn)Te single crystal X-ray detector, 4 times that of α-Se X-ray detectors, and 70 times that of polycrystalline perovskite X-ray detectors.[16] In the same year, Kovalenko's group demonstrated that solution-grown $MAPbI_3$, $FAPbI_3$, and I-treated $MAPbBr_3$ single crystals could serve as room-temperature, direct-conversion solid-state gamma-detecting materials. They further noted that although $FAPbI_3$ single crystal exhibits thermodynamic instability, it is still viable for the testing, and

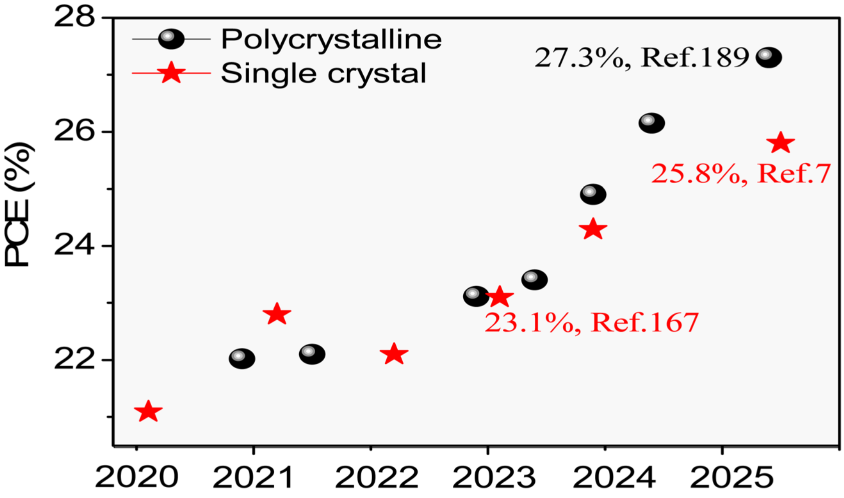

Fig. 17 Notable efficiency evolution of single-junction p–i–n perovskite polycrystalline and single-crystal solar cells since 2020.[189–197] Copyright 2025, Progress in Photovoltaics: Research and Applications.

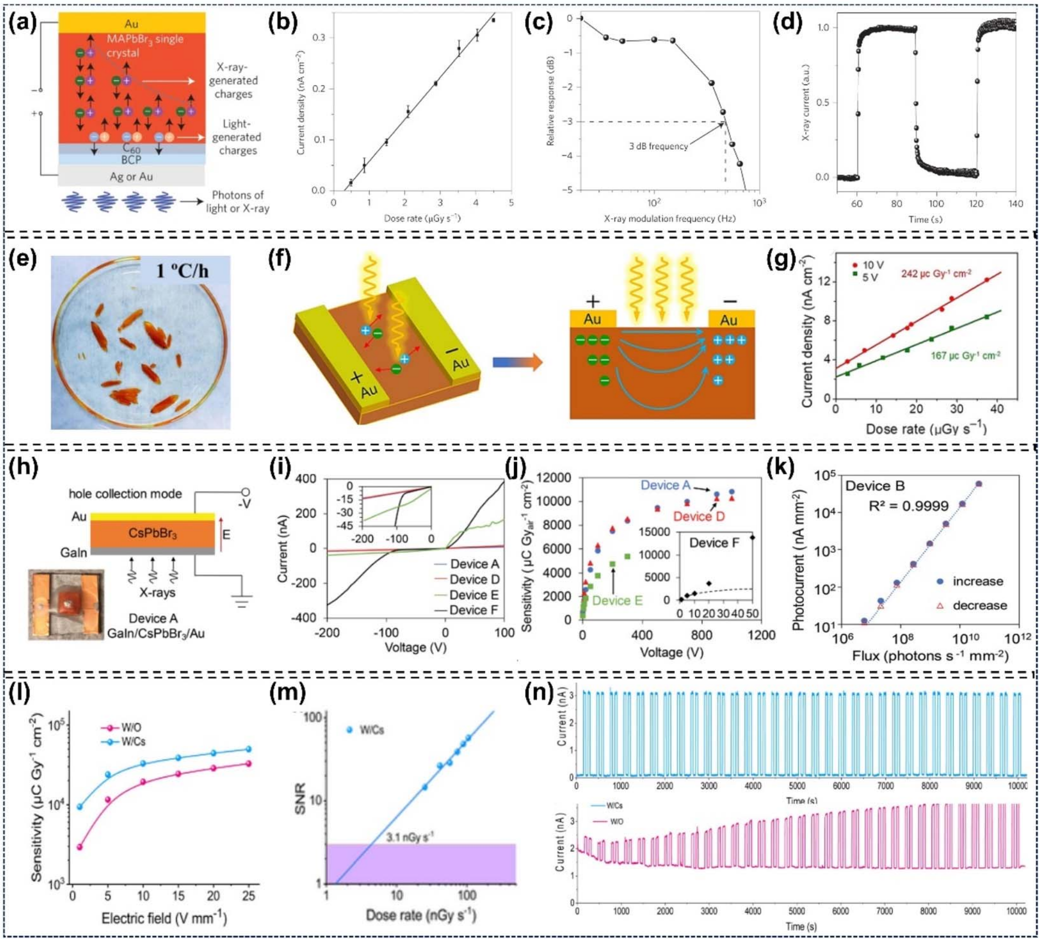

Fig. 18 Characteristics of single-crystal perovskite-based X-ray detectors: (a–d) device architecture and performance metrics of single-crystalline perovskite X-ray detectors.[16] Copyright 2016, Springer Nature. (e) Photograph of (BDA)PbI$_4$ single crystals grown at 30 °C min^{-1} ramp rate; (f) schematic of planar X-ray detector geometry and electric field distribution; (g) X-ray induced response current across varying dose rates, with sensitivity extracted from the slope of the linear fit.[159] Copyright 2020, Wiley-VCH. (h) Schematic of the CsPbBr$_3$ detector structure and experimental test configuration; (i–k) dark *I*–*V* characteristics, X-ray sensitivity, and photocurrent calculations under different X-ray flux conditions for CsPbBr$_3$ devices.[160] Copyright 2023, Wiley-VCH. (l–n) Comparative analysis of sensitivity, SNR, and X-ray on/off response currents for W/Cs SC and W/O SC detectors.[161] Copyright 2025, Wiley-VCH.

detectors based on FAPbI$_3$ showed optimal detection performance.[157] Concurrently, Wei *et al.* obtained a high resolution ^{137}Cs gamma-ray energy spectrum using an MAPbBr$_{2.94}$Cl$_{0.96}$ single-crystal detector under a modest electric field of 1.8 V mm^{-1} at room temperature. The spectral resolution surpassed that of conventional scintillator-based detectors.[158] Additionally, Liu *et al.* developed a high sensitivity X-ray detector based on the (BDA)PbI$_4$ (BDA = NH$_3$C$_4$H$_8$NH$_3$) single crystal synthesized in aqueous solution *via* a modified temperature crystallization method. The Schottky-type detector exhibited a remarkable sensitivity of 242 μC Gy$_{\text{air}}$$^{-1}$ cm^{-2} under a 10 V bias (0.31 V μm^{-1}), surpassing Pb-free Cs$_2$AgBiBr$_6$ (105 μC Gy$_{\text{air}}$$^{-1}$ cm^{-2}, 25 V mm^{-1}) and MAPbBr$_3$ single crystals (80 μC Gy$_{\text{air}}$$^{-1}$ cm^{-2}) by factors of 2.3 and 3.0, respectively (Fig. 18e–g).[159] Subsequently, the Kanatzidis research group demonstrated an all-inorganic CsPbBr$_3$ single crystal detector fabricated through a low-cost solution growth process, achieving superior material quality characterized by low defect density and excellent short-range order. The eutectic gallium indium/CsPbBr$_3$/Au Schottky diode structure attained a record-high X-ray sensitivity exceeding 10 000 μC Gy$_{\text{air}}$$^{-1}$ cm^{-2} with an ultra-low detection limit of 22 nGy$_{\text{air}}$ s^{-1}. Notably, the device maintained excellent photocurrent linearity and reproducibility under synchrotron X-ray irradiation (58.61 keV, 10^6–10^{10} photons s^{-1} mm^{-2}), demonstrating its operational stability in extreme radiation environments (Fig. 18h–k).[160] In a recent breakthrough, Liu *et al.* demonstrated Cs$^+$-doped MAPbI$_3$ single crystals exhibiting superior X-ray detection performance through systematic investigation of dopant-induced modifications in crystal lattice symmetry, defect population distribution, bandgap alignment, ion migration barriers, and carrier transport kinetics. The fabricated detectors achieved unprecedented detection metrics, including a high sensitivity of 49 847 μC Gy$_{\text{air}}$$^{-1}$ cm^{-2}, low detection limit of 3.1 nGy$_{\text{air}}$ s^{-1}, short response rise time of 150 μs, coupled with exceptional long-term stability (>10 000 s continuous operation under X-ray irradiation and bias) as evidenced by the invariant response current curves shown in Fig. 18l–n.[161]

X-ray detectors are categorized into two types: direct and indirect. Direct detectors utilize ionized materials to convert high-energy radiation directly into electrical signals. Indirect detectors, by contrast, employ scintillators to transform X-rays into low-energy photons, which are subsequently captured by an arrayed photodetector to produce imaging. In 2016, Birowosuto and colleagues conducted a study on the X-ray scintillation properties of (EDBE)$PbCl_4$, $MAPbI_3$ and $MAPbBr_3$ single crystals. Through low temperature X-ray excited luminescence measurements, they discovered that the X-ray luminescence yield could reach up to approximately 1 20 000 photons per MeV for (EDBE)$PbCl_4$ at a temperature of 130 K, and exceed 1 50 000 photons per MeV for both $MAPbI_3$ and $MAPbBr_3$ at 10 K. Notably, the light yield of the 3D perovskites $MAPbI_3$ and $MAPbBr_3$ dropped sharply at room temperature, falling below 1000 photons per MeV, whereas the 2D perovskite (EDBE)$PbCl_4$ was less affected, maintaining a yield of around 9000 photons per MeV (Fig. 19a–c). This significant temperature dependence is attributed to the thermal quenching behavior in the 3D perovskite, while the 2D perovskite mitigates this effect due to its large exciton binding energy.[162] Subsequently, Xu's team investigated the room temperature scintillation properties of $MAPbCl_{3-x}Br_x$ crystals, and identified that those with high emission-weighted longitudinal transmittance (EWLT) hold promise for scintillator applications.[163–165] Specifically, the $MAPbBr_{0.05}Cl_{2.95}$ crystal exhibits an outstanding EWLT of 90%, significantly outperforming the 57.2% EWLT achieved by LYSO. Moreover, this crystal demonstrates a superior light yield of 18 000 photons per MeV and an exceptionally short decay time of 0.14 ± 0.02 ns, surpassing the $MAPbCl_3$ crystal in these aspects (Fig. 19d–f).[166] Additionally, a formic acid-assisted metastable crystallization approach was proposed by Zhu *et al.* for the fabrication of high-quality $MAPbBr_3$ single crystals. The X-ray detectors constructed from these crystals exhibit a remarkable sensitivity of 2975.7 $\mu C\ Gy_{air}^{-1}\ cm^{-2}$ under a −20 V bias, coupled with a minimal detectable X-ray dose rate of 0.48 μGy_{air}^{-1}, which is approximately 11 times lower than the threshold value of 5.5 μGy_{air}^{-1} required for routine medical diagnostic applications.[167] Liu *et al.* proposed an airflow-controlled solvent evaporation (ACSE) strategy for the room-temperature growth of large-sized 2D layered perovskite $(PEA)_2PbBr_4$ single crystals, and systematically investigated their X-ray scintillation performance. Under X-ray excitation, the $(PEA)_2PbBr_4$ single crystal demonstrates a high light yield of 73 226 photons per MeV and a fast response time of 14 ns, which are approximately 1.4 times and 75 times superior to those of the commercial CsI:Tl scintillator (54 000 photons per MeV and 1049 ns), respectively. Based on these prominent characteristics, an X-ray imager was constructed by integrating a $(PEA)_2PbBr_4$ single crystal, achieving a high spatial resolution of 11.1 lp mm^{-1} in X-ray imaging (Fig. 19g–i).[168] Meanwhile, Song *et al.* reported a novel scintillation material, namely $CsPbCl_xBr_{3-x}:Yb^{3+}$ quantum cutting scintillator, which features a PLQY of 149% and a Stokes shift exceeding 550 nm. This material successfully overcomes the issues of poor PLQY caused by thermal quenching and large self-absorption in 3D perovskite SCs. Moreover, the scintillators exhibit high transmittance, large X-ray absorption/conversion efficiency, an outstanding light yield of 1 12 281 photons per MeV, and a detection limit as low as 176.5 $nGy_{air}\ s^{-1}$, and enable high-contrast single-pixel X-ray imaging (Fig. 19j and k).[169] Recently, Gao *et al.* prepared a series of deuterated $MAPbI_3$-based X-ray detectors (D_xMAPbI_3, $x = 0, 0.15, 0.75, 0.99$), and improved their performances by tuning deuterium content in organic cations. The $D_{0.99}MAPbI_3$ SC detector exhibits a more than five-fold performance enhancement, featuring a record $\mu\tau$ product ($5.39 \times 10^{-2}\ cm^2\ V^{-1}$), ultrahigh sensitivity ($2.18 \times 10^6\ \mu C\ Gy^{-1}\ cm^{-2}$ at 120 keV), low detection limit (4.8 $nGy_{air}\ s^{-1}$) and long-term stability, offering a straightforward route to advanced perovskite X-ray detection systems.[170] Zhao and his research team made a notable breakthrough by successfully synthesizing inch-sized $(PEA)_2PbBr_4$ SCs (4.60 cm ×3.80 cm ×0.19 cm) using a combined approach of evaporation crystallization and nucleation-controlled strategies. These $(PEA)_2PbBr_4$ SCs demonstrated exceptional scintillation performance, characterized by high light yields of 38 600 photons per MeV and ultra-fast decay times (4.89 ns under a 375 nm laser, 27.98 ns under γ-ray exposure, and 3.84 ns under α-particle bombardment). For X-ray imaging, the $(PEA)_2PbBr_4$ SCs achieved a spatial resolution of 23.2 lp mm^{-1} at a modulation transfer function of 20%. Additionally, they set a record resolution of 2.00 lp mm^{-1} for fast neutron imaging, marking the highest resolution achieved by perovskite scintillators to date (Fig. 19l and m). X-ray imaging tests were conducted using a ballpoint pen, a 2.72 cm spring, and a 0.60 cm spring, all encapsulated within a polytetrafluoroethylene triangular prism as test objects. As illustrated in Fig. 19n, the radiographs clearly depicted the ballpoint pen tip and the springs, highlighting the outstanding non-destructive detection capabilities of the $(PEA)_2PbBr_4$ SCs.[171]

4.4. Light-emitting diodes and lasers

Lead halide perovskite single crystals excel as high-performance light-absorbing materials, with broad application prospects not only in solar cells and photodetectors but also across diverse optoelectronic fields such as light-emitting diodes (LEDs) and lasers. This exceptional versatility stems primarily from their superior photoluminescence efficiency, low bulk defect density, suppressed Auger recombination rates, and ability for long-range, balanced ambipolar charge transport. The research on single-crystal perovskite light-emitting diodes (PeLEDs) originated in 2014, when Tan *et al.* first reported green and red light-emitting devices based on $CH_3NH_3PbI_{3-x}Cl_x$ perovskite.[172] Since then, extensive efforts have been devoted to enhancing the quantum efficiency of PeLEDs, including optimizing the crystalline quality of the perovskite luminescent layer and improving the performance of electron/hole transport layers.[57,173–176] However, PeLED development is significantly constrained by incoherent light emission arising from random

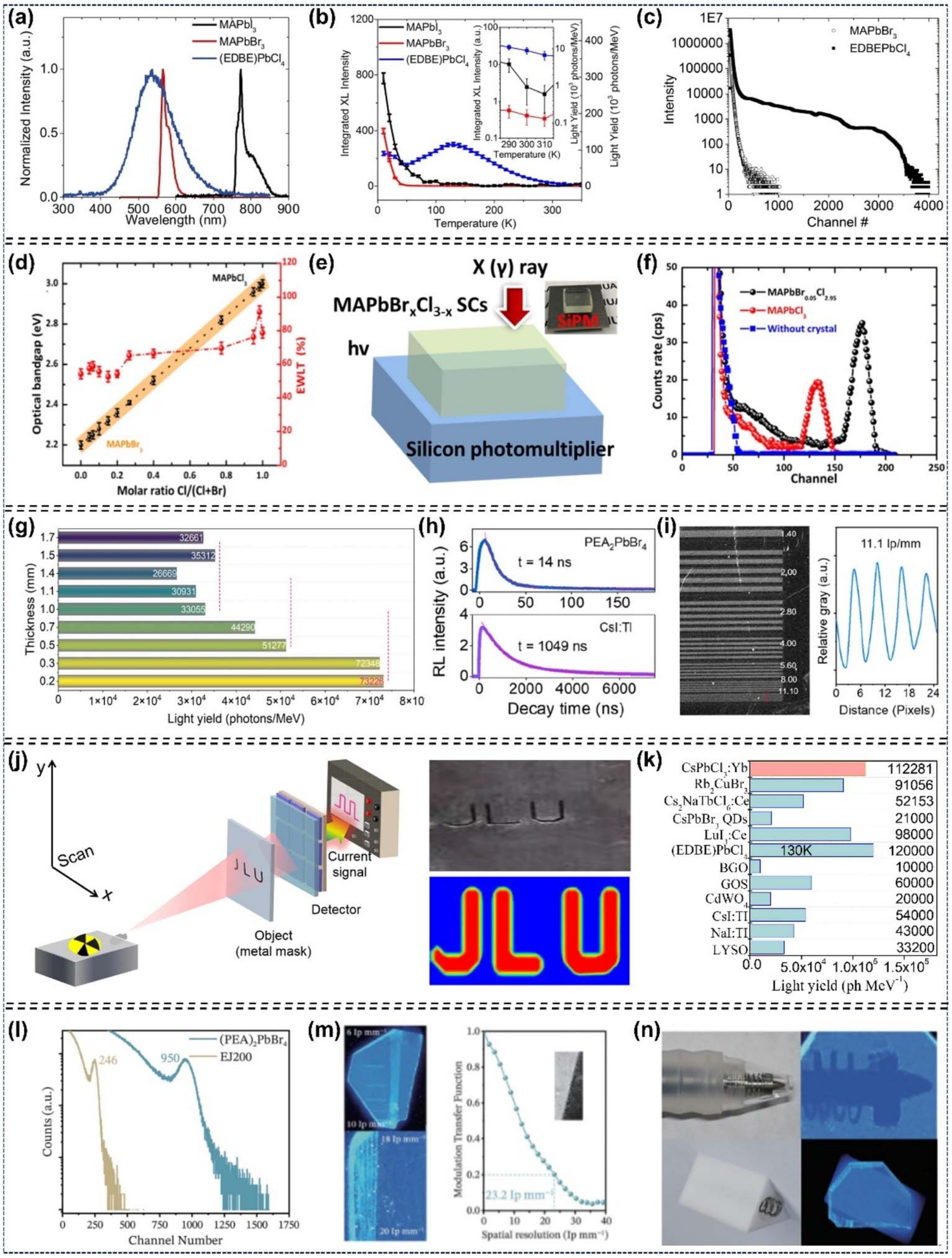

Fig. 19 Scintillation properties of single-crystal perovskites: (a–c) comparison of normalized X-ray excited luminescence spectra, light yield temperature dependence, and pulse height spectra.[162] Copyright 2016, Springer Nature. (d) Optical band gap, integrated XEL light yield, and EWLT *versus* Cl/(Br + Cl) molar ratio; (e and f) pulse height spectra and schematic of MAPbBr$_x$Cl$_{3-x}$ SCs integrated on the window of SiPM.[166] Copyright 2018, American Chemical Society. (g–i) Light yield SC thickness dependence, RL decay time, and X-ray line chart image of the (PEA)$_2$PbBr$_4$ scintillator.[168] Copyright 2023, American Chemical Society. (j and k) Single pixel X-ray imaging and light yield of CsPbCl$_3$:Yb^{3+} scintillators.[169] Copyright 2023, Wiley-VCH. (l–n) Pulse height spectra, modulation transfer function curves, photographs and X-ray images of encapsulated objects.[171] Copyright 2025, Wiley-VCH.

crystal domain orientations in polycrystalline perovskite thin films. Consequently, single-crystal perovskite-based LEDs demand urgent development, serving as a crucial milestone for electrically driven laser diodes.[177]

In 2015, the Gao group successfully fabricated efficient and bright green LEDs utilizing single-crystalline, highly emissive MAPbBr$_3$ nanoplatelets. This achievement was primarily attributed to the inherent properties of the single-crystal nanoplatelets and the introduction of composition-tailored bipolar host materials. Further investigation revealed that the as-prepared perovskite nanomaterials exhibited high stability and moisture resistance in ambient air, enabling glovebox-free fabrication of LED devices.[178] Subsequently, Yu's group designed LEDs based on perovskite single-crystalline microplatelets, adopting a simple ITO/MAPbBr$_3$/Au device structure. This device could be turned on at 1.8 V and operate for 54 h

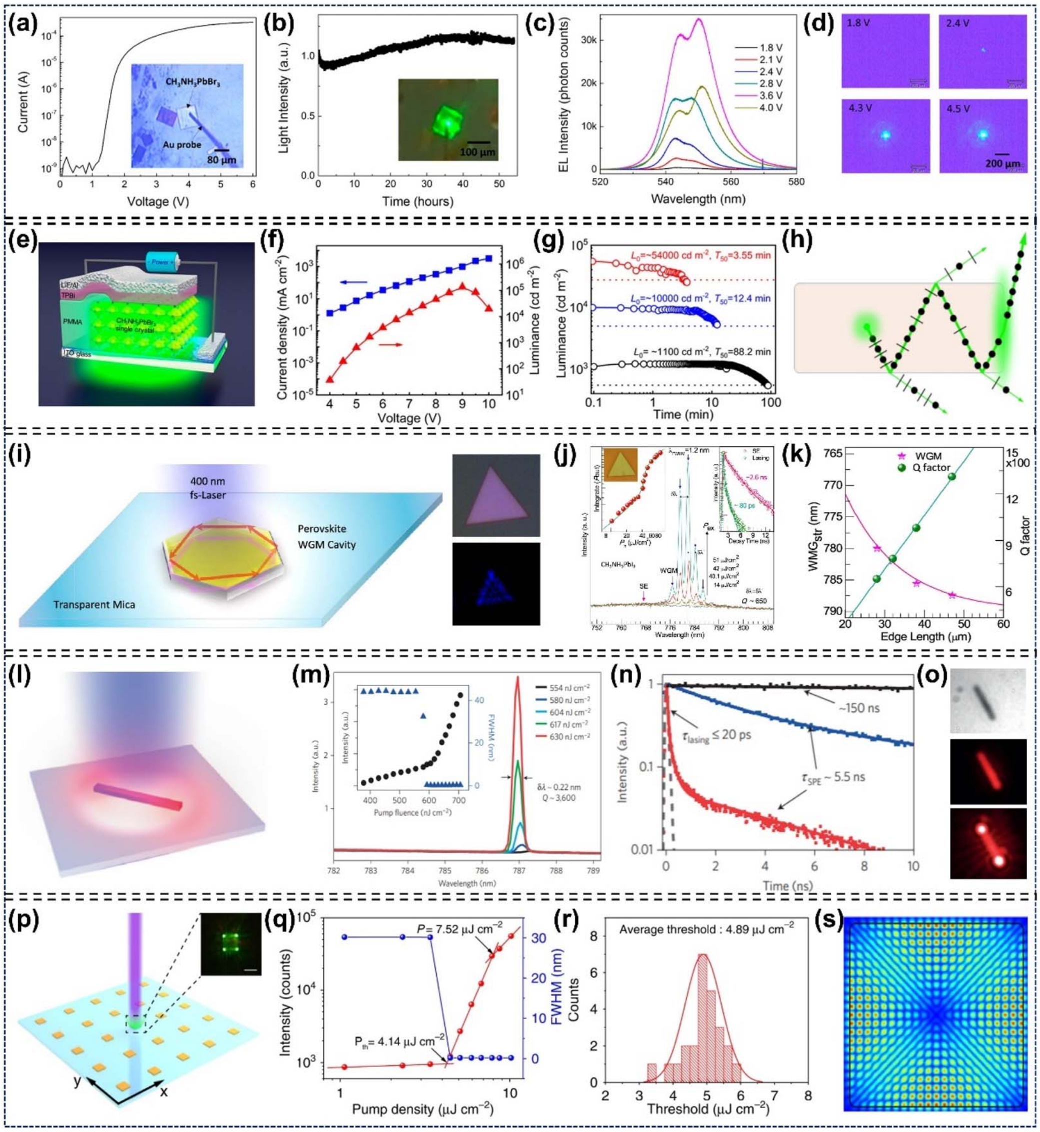

Fig. 20 Characteristics of single-crystal perovskite-based LEDs and lasers: (a–d) I–V curve, stability pattern, electroluminescence spectra, and microscopic optical images of an $MAPbBr_3$ microplatelet-based LED.[177] Copyright 2017, American Chemical Society. (e–h) Device construction, L–V–J curves, operational stability, and schematic of polarized emission generation for PSC-LEDs.[180] Copyright 2022, American Chemical Society. (i–k) Schematic illustration of perovskite whispering-gallery-mode nanocavities and their corresponding lasing characterization.[186] Copyright 2014, American Chemical Society. (l–o) Schematic illustration, lasing threshold emission spectra, optical images, and time resolved photoluminescence decay kinetics of near-infrared lasing from single crystal $MAPbI_3$ nanowires.[15] Copyright 2015, Springer Nature. (p) Schematic illustration of an individual $MAPbBr_3$ microplate excited by a 395 nm laser; (q) integrated PL emission intensity (red) and FWHM (blue) of PL peaks *versus* pump density; (r) lasing threshold statistics of $MAPbBr_3$ microplate arrays; (s) FDTD simulations of whispering gallery modes.[187] Copyright 2023, Springer Nature.

under a luminance of approximately 5000 cd m^{-2} without any noticeable degradation in brightness (Fig. 20a–d).[177] Nguyen *et al.* fabricated a green luminescence device with a simple ITO/$MAPbBr_3$/ITO structure. The finding of photoluminescence blinking behavior at the crystal edges may provide new insights into the recombination processes depending on the carrier traps and defects of emission layers in perovskite light-emitting devices.[178] Simultaneously, Gao *et al.* obtained a high quality $MAPbBr_3$ film consisting of micron-scale single crystals by utilizing benzophenone as a crystallizing agent, and applied this film to PeLED fabrication. Compared with the control device, the device showed enhanced performance, achieving a maximum luminance of 1057.6 cd m^{-2} and a turn-on voltage of 2.25 V.[179] Recently, Jie *et al.* proposed a convenient and efficient liquid-insulator bridging strategy to fabricate high-luminance green PSC-based LEDs using $CH_3NH_3PbBr_3$ microflakes. A blade-coated poly(methyl methacrylate) insulating layer mitigated leakage current and short circuits, enabling reliable PSC-LED fabrication. The device exhibited an ultrahigh luminance of 1 36 100 cd m^{-2} and a half-lifetime of 88.2 min at an initial luminance of ∼1100 cd m^{-2}. Additionally, the microflake-based PSC-LEDs exhibited strong polarized edge emission with a high degree of polarization reaching up to 0.69 (Fig. 20e–h).[180] Meanwhile, Chen *et al.* developed an LED based on bare perovskite single-crystal films that achieved high performance without relying solely on surface passivation and interface modification. The device achieved a brightness exceeding 10 000 cd m^{-2} and an EQE of ~1.3%. Moreover, their electroluminescence peak was centered at 521 nm with a full width at half maximum of 18 nm, which fully meets the display requirements of the National Television System Committee standard. The device also exhibited good stability, their T_{50} reached over 2 h and 37 h at 1000 cd m^{-2} and 100 cd m^{-2} initial luminance, respectively.[181]

Lead halide perovskite single crystals have low trap state density, long electron–hole diffusion length, high carrier mobility, and extended carrier lifetime, making them ideal for laser devices with low lasing thresholds and high qualities.[15,41,182,184] For example, Hou *et al.* devised an antisolvent-free strategy for fabricating $MAPbBr_3$ single-crystal microdisks with square and octagonal morphologies. Specifically, a trace amount of *N*-methyl-2-pyrrolidone (NMP) was incorporated into the perovskite precursor solution to decelerate the crystallization kinetics during spin-coating. The resultant $MAPbBr_3$ microdisks enabled whispering gallery mode (WGM) lasing, exhibiting excellent laser performance with a threshold value below 50 mJ cm^{-2} and a quality factor exceeding 1000.[183] Yan *et al.* prepared $MAPbBr_3$ single-crystal microcavities by integrating template-limited growth with antisolvent diffusion methods, yielding microcavities with tunable geometries and sizes. These single-crystal microcavities emitted laser light at ≈550 nm under femtosecond laser pumping, displaying a lasing threshold of ≈35 μJ cm^{-2}, a quality factor of 1135, as well as outstanding long-term operational stability.[184] Recently, Sum group's research revealed that $MAPbX_3$ (X = Cl, Br, I) perovskites serve as highly promising gain media, endowed with a range of desirable properties. Notably, lasing behavior in $MAPbI_3$ single crystals was successfully induced through the utilization of specifically designed cavity resonators. Furthermore, the inherently low bulk defect density characteristic of $MAPbI_3$ films plays a pivotal role in achieving reduced amplified spontaneous emission thresholds, alongside facilitating long-range, balanced charge carrier diffusion lengths.[185] Subsequently, Xiong's group has made significant advancements in the realm of low-threshold NIR nanolasers, successfully realizing NIR lasing by employing $CH_3NH_3PbI_{3-a}X_a$ (X = Cl, Br, I) nanoplatelets integrated within a distributed Bragg reflector (DBR) cavity. Notably, their experiments showed a typical $MAPbI_3$ triangular nanoplatelet with a low lasing threshold of 37 μJ cm^{-2} and a quality factor of 650 (Fig. 20i–k).[186] Adopting a similar approach, Liao *et al.* designed a novel single-crystalline laser, which utilizes the four side faces of square $MAPbBr_3$ microdisks as a built-in whispering-gallery mode microresonator. This laser achieved a low threshold of 3.6 μJ cm^{-2}, a quality factor of 430, and emitted light at a wavelength of 557.5 nm from the four side-faces of the square $MAPbBr_3$ microdisk.[146] Additionally, the Zhu group developed wavelength-tunable single crystal $MAPbX_3$ (X = Br, I) nanowire lasers, with a threshold of 220 nJ cm^{-2} and a quality factor of 3600 (Fig. 20l–o).[15] Jin's group successfully prepared high-quality $FAPbX_3$ (X = Br, I) and MABr-stabilized $FAPbI_3$ single-crystal nanowires *via* low-temperature solution growth. These nanowires showed superior photostability and longer wavelength tunability compared to MA-based perovskites, and the corresponding nanowire exhibited a lasing threshold of approximately several μJ cm^{-2} and a quality factor of ~2000.[17] Recently, Pan *et al.* successfully synthesized high-quality single-crystalline $MAPbBr_xCl_{3-x}$ ($MA = CH_3NH_3$, $x = 0, 1, 2, 3$) microplate arrays. These perovskite microplates serve as high-quality microcavities for whispering gallery mode lasing, demonstrating a high-quality factor of 2915 and a low threshold of 4.14μJ cm^{-2}. Importantly, the lasing mode can be precisely tuned by adjusting the dimensions of the microplates (Fig. 20p–s).[187] In a separate study, Chen *et al.* developed a high-performance vertical cavity surface emitting laser (VCSEL) *via* a simple solution process. The device uses a highly crystalline $CsPbBr_3$ single-crystal microplatelet, which is sandwiched between two distributed Bragg reflector. Under 400 nm femtosecond optical pumping, this VCSEL achieves single-mode lasing at 542 nm, with a low threshold power density of 5 μJ cm^{-2} and a high-quality factor of 2893.[188]

5. Conclusion and outlook

In this review, we present a thorough overview of the remarkable advancements achieved in the field of lead halide perovskite single crystals, encompassing their fundamental properties, growth techniques, and device applications. Numerous studies have confirmed that single-crystalline perovskites outperform polycrystalline thin-film counterparts in terms of photoelectric performance, primarily due to their extremely low defect densities and few interface defects. Moreover, these materials exhibit superior thermal and ambient stability, rendering them ideal candidates for high-stability optoelectronic devices while enabling in-depth exploration of the intrinsic properties of perovskite materials. Nevertheless, several long-standing challenges in this field remain to be addressed and overcome by researchers. We believe that in-depth research into the following aspects will provide researchers with substantial benefits and innovative insights, driving performance optimization of single-crystalline perovskites and accelerating the development of related optoelectronic devices.

(1) Manufacturing challenges: compared to bulk single-crystal perovskites, single-crystalline thin films are better suited for direct use in a wide range of vertical-type optoelectronic devices. However, the preparation of single-crystalline perovskite thin films that simultaneously feature submicron thickness and large lateral dimensions continues to pose a significant challenge. Initially, researchers adopted a slicing process to obtain the desirable materials, but this method led to serious material loss and required multiple necessary post-treatment processes. Later, the space confinement method emerged as an efficient alternative, yet it has drawbacks, such as extensive organic solvent use and difficulty in accurately controlling nucleation rate. Therefore, a dual-pronged strategy is imperative to fabricate high-quality single-crystalline perovskite thin films with precisely controllable

morphology and dimensions going forward. On the one hand, new and universal growth methods tailored specifically to these thin films should be vigorously explored and developed. On the other hand, the refinement and upgrading of immature solution-based techniques are of equal importance, which entails innovating and optimizing the instrumentation for space-confined single crystal growth, as well as leveraging template-seeded directional growth strategies to precisely modulate the thickness and dimensions of the target thin films, thereby satisfying the stringent requirements of advanced optoelectronic applications.

(2) Defects and nonradiative carrier losses: with inherent merits including ultralow defect density, extended carrier diffusion length and elevated ion migration barrier, single-crystal perovskites exhibit immense potential in diverse optoelectronic applications. Although significant breakthroughs have been realized in high-energy ray detectors and laser technologies, the efficiency of single-crystal perovskite solar cells remains inferior to that of polycrystalline thin-film solar cells. This efficiency disparity is primarily attributable to the high surface/interface defect states in single-crystal perovskites, as well as the incomplete interface contact between the perovskite layer and charge transport layers/substrate, both of which induce carrier nonradiative recombination and consequent efficiency loss. Accordingly, the following targeted strategies can be implemented to elevate the efficiency of perovskite single-crystal solar cells. (i) Devise effective surface passivation approaches, such as using organic cations to passivate the uncoordinated halogen or lead ion defects on the crystal surface. (ii) Adopt appropriate additives and nucleation technologies, for instance, regulating crystal growth by leveraging Lewis acids and bases; alternatively, enabling *in situ* nucleation and growth of crystals with organic amine salts (*e.g.*, PEA^+, EA^+, NHMS and $FCNO_2$) to reduce defects. (iii) Optimize device fabrication processes to enhance the contact between single-crystal perovskites and substrates, such as suppressing the carrier recombination loss in single-crystal devices *via* doping, energy level optimization, surface/interface defect passivation and other related methods.

(3) Stability issues: it is of utmost importance to thoroughly address the challenges related to long-term stability, encompassing both thermal and environmental stability, in perovskite-based optoelectronic devices. Although compared with perovskite polycrystalline thin films, single-crystalline perovskite exhibited better performance through applying the interface engineering and passivating technique, they remain limited by insufficient long-term stability. Future research should prioritize the development of stable perovskite compositions, which includes constructing mixed-halides (*e.g.*, $MAPb(Br/I)_3$) or mixed-cation (*e.g.*, $(Cs/FA)_1PbI_3$) single-crystal systems or incorporating anti-degradation stabilizing additives. A deeper insight into degradation pathways, especially halide ion migration and phase transition, is essential for enhancing long-term stability. Given the critical impact of lattice defects on material stability, exploring defect-mitigation strategies (*e.g.*, doping organic cations, Lewis acids/bases, and optimizing precursor solution concentration) will underpin the practical long-term application of perovskite materials. Additionally, the inherent toxicity concerns associated with Pb-based perovskites warrant careful and comprehensive consideration. This issue constitutes the most formidable barrier that hinders their large-scale commercialization. Consequently, there is an urgent demand for Pb-free, low-toxicity single-crystal perovskites with robust long-term stability in the highly efficient photoelectric device field.

(4) Device integration difficulties: single-crystal perovskite materials have a defect density two to three orders of magnitude lower than that of their polycrystalline counterparts, positioning them as a highly promising light-absorbing layer for photovoltaic applications. Nevertheless, the PCE of solar cells based on single-crystal perovskites currently falls short of that achieved by their polycrystalline counterparts. This efficiency gap primarily stems from the relatively late development of single-crystal materials, which renders their integration with established photovoltaic technologies highly challenging. The structural design of existing high-efficiency perovskite solar cells, along with the selection of electrode and charge transport layer materials, is optimized primarily for polycrystalline perovskite materials and their charge transport characteristics. Although single-crystal perovskites possess superior charge mobility and longer carrier lifetime, mismatched energy levels and high interfacial barriers in the current device structures fail to exploit these advantages, limiting charge extraction and collection efficiency. Therefore, future research should focus on designing device structures tailored to the characteristics of single crystals. Specifically, based on the unique charge transport properties of single-crystal perovskites, charge transport layer materials with matched energy levels need to be selectively adopted and the thickness and doping concentration of the transport layers adjusted. Meanwhile, novel device architecture such as the p–i–n inverted structure needs to be explored to accelerate the rate of charge extraction and collection, giving full play to the advantages of low defect density in single-crystal materials. Furthermore, single crystal preparation equipment compatible with existing polycrystalline production lines should be developed to reduce production line transformation costs.

Author contributions

All of the authors contributed to the literature search, writing and editing of this review.

Conflicts of interest

There are no conflicts to declare.

Data availability

No primary research results, software, or code have been included, and no new data were generated or analysed as part of this review.

Acknowledgements

This work was supported by the National Natural Science Foundation of China (Grant No. 12404458, 62222502, and U2441222), the Natural Science Foundation of Inner Mongolia

(2024QN02025), the Key Scientific Research Project Plan of Colleges and Universities in Henan Province (25A140016), the “Yingcai Xingmeng” Team Project (No. 2025TYL06), and Research Foundation for Advanced Talents of Inner Mongolia Normal University (2025YJRC011).

References

1 H. L. Wells, *Z. Anorg. Allg. Chem.*, 1893, **3**, 195–210.
2 H. F. Kay and P. C. Bailey, *Acta Cryst.*, 1957, **10**, 219–226.
3 J. Chen and N. G. Park, *Adv. Mater.*, 2019, **31**, 1803019.
4 J. Ding and Q. Yan, *Sci. China Mater.*, 2017, **60**, 1063–1078.
5 T. Leijtens, E. T. Hoke, G. Grancini, D. J. Slotcavage, G. E. Eperon, J. M. Ball, M. D. Bastiani, A. R. Bowring, N. Martino, K. Wojciechowski, M. D. McGehee, H. J. Snaith and A. Petrozza, *Adv. Energy Mater.*, 2015, **5**, 1500962.
6 J. Z. Song, Q. Z. Cui, J. H. Li, J. Y. Xu, Y. Wang, L. M. Xu, J. Xue, Y. H. Dong, T. Tian, H. D. Sun and H. B. Zeng, *Adv. Opt. Mater.*, 2017, **5**, 1700157.
7 N. Q. Liu, M. X. Liu, J. T. Dai, X. Cheng and Z. L. Chen, *Angew. Chem., Int. Ed.*, 2025, **64**, e202500947.
8 Z. Z. Chang, Z. J. Lu, W. Deng, Y. D. Shi, Y. Y. Sun, X. J. Zhang and J. S. Jie, *Nanoscale*, 2023, **15**, 5053–5062.
9 N. Ding, H. L. Liu, Y. Q. Liu, D. G. Li, M. Y. Yao, Y. N. Ji, G. Zhu, R. Xue and W. Xu, *Laser Photonics Rev.*, 2025, 202500887.
10 K. Grover, J. S. Choudhary, P. Dhawan, R. Jha and H. Yadav, *J. Phys. Chem. Solids*, 2025, **203**, 112713.
11 R. H. Mao, L. Y. Zhang and R. Y. Zhu, *IEEE Trans. Nucl. Sci.*, 2012, **59**, 2224–2228.
12 Q. Xu, H. T. Wei, W. Wei, W. Chuirazzi, D. DeSantis, J. S. Huang and L. Cao, *Nucl. Instrum. Methods Phys. Res. A*, 2017, **848**, 106–108.
13 H. J. Fang, Q. Li, J. Ding, N. Li, H. Tian, L. J. Zhang, T. L. Ren, J. Y. Dai, L. D. Wang and Q. F. Yan, *J. Mater. Chem. C*, 2016, **4**, 630–636.
14 B. W. H. Baugher, H. O. H. Churchill, Y. F. Yang and P. J. Herrero, *Nat. Nanotechnol.*, 2014, **9**, 262–267.
15 H. M. Zhu, Y. P. Fu, F. Meng, X. X. Wu, Z. Z. Gong, Q. Ding, M. V. Gustafsson, M. T. Trinh, S. Jin and X. Y. Zhu, *Nat. Mater.*, 2015, **14**, 636–642.
16 H. T. Wei, Y. J. Fang, P. Mulligan, W. Chuirazzi, H. H. Fang, C. C. Wang, B. R. Ecker, Y. L. Gao, M. A. Loi, L. Cao and J. S. Huang, *Nat. Photonics*, 2016, **10**, 333–339.
17 Y. P. Fu, H. M. Zhu, A. W. Schrader, D. Liang, Q. Ding, P. Joshi, L. Hwang, X. Y. Zhu and S. Jin, *Nano Lett.*, 2016, **16**, 1000–1008.
18 F. Cao, J. D. Chen, D. J. Yu, S. Wang, X. B. Xu, J. X. Liu, Z. Y. Han, B. Huang, Y. Gu, K. L. Choy and H. B. Zeng, *Adv. Mater.*, 2020, **32**, 1905362.
19 J. M. Chen, R. H. Mao, L. Y. Zhang and R. Y. Zhu, *IEEE Trans. Nucl. Sci.*, 2007, **54**, 718–724.
20 X. Gong, M. H. Tong, Y. J. Xia, W. Z. Cai, J. S. Moon, Y. Cao, G. Yu, C. L. Shieh, B. Nilsson and A. J. Heeger, *Science*, 2009, **325**, 1665–1667.
21 J. H. Noh, S. H. Im, J. H. Heo, T. N. Mandal and S. I. Seok, *Nano Lett.*, 2013, **13**, 1764–1769.
22 J. S. Park, S. Choi, Y. Yan, Y. Yang, J. M. Luther, S. H. Wei, P. Parilla and K. Zhu, *J. Phys. Chem. Lett.*, 2015, **6**, 4304–4308.
23 C. Rodà, A. L. Abdelhady, J. Shamsi, M. Lorenzon, V. Pinchetti, M. Gandini, F. Meinardi, L. Manna and S. Brovrlli, *Nanoscale*, 2019, **11**, 7613–7623.
24 J. N. Chen, S. S. Zhou, S. Y. Jin, H. Q. Li and T. Y. Zhai, *J. Mater. Chem. C*, 2016, **4**, 11–27.
25 H. W. Zhou, Z. H. Nie, J. Yin, Y. W. Sun, H. Y. Zhuo, D. Q. Wang, D. C. Li, J. M. Dou, X. X. Zhang and T. L. Ma, *RSC Adv.*, 2015, **5**, 85344–85349.
26 M. Y. Luan, J. L. Song, X. F. Wei, F. Chen and J. H. Liu, *CrystEngComm*, 2016, **18**, 5257–5261.
27 Y. Tidhar, E. Edri, H. Weissman, D. Zohar, G. Hodes, D. Cahen, B. Rybtchinski and S. Kirmayer, *J. Am. Chem. Soc.*, 2014, **136**, 13249–13256.
28 M. Y. Chen, H. Yu, S. V. Kershaw, H. H. Xu, S. Gupta, F. Hetsch, A. L. Rogach and N. Zhao, *Adv. Funct. Mater.*, 2014, **24**, 53–59.
29 Q. Q. Lin, A. Armin, P. L. Burn and P. Meredith, *Laser Photonics Rev.*, 2016, **10**, 1047–1053.
30 C. X. Bao, Z. L. Chen, Y. J. Fang, H. T. Wei, Y. H. Deng, X. Xiao, L. L. Li and J. S. Huang, *Adv. Mater.*, 2017, **29**, 1703209.
31 B. C. Yu, J. J. Shi, Y. M. Li, S. Tan, Y. Q. Cui, F. Q. Meng, H. J. Wu, Y. H. Luo, D. M. Li and Q. B. Meng, *Nat. Commun.*, 2025, **16**, 3328.
32 M. J. Yang, Y. Y. Zhou, Y. N. Zeng, C. S. Jiang, N. P. Padture and K. Zhu, *Adv. Mater.*, 2015, **27**, 6363–6370.
33 Y. H. Zhang, R. J. Sun, X. Y. Ou, K. F. Fu, Q. S. Chen, Y. C. Ding, L. J. Xu, L. M. Liu, Y. Han, A. V. Malko, X. G. Liu, H. H. Yang, O. M. Bark, H. Liu and O. F. Mohammed, *ACS Nano*, 2019, **13**, 2520–2525.
34 H. Deng, X. K. Yang, D. D. Dong, B. Li, D. Yang, S. J. Yuan, K. Qiao, Y. B. Cheng, J. Tang and H. S. Song, *Nano Lett.*, 2015, **15**, 7963–7969.
35 H. S. Rao, B. X. Chen, X. D. Wang, D. B. Kuang and C. Y. Su, *Chem. Commun.*, 2017, **53**, 5163–5166.
36 Y. X. Chen, Q. Q. Ge, Y. Shi, J. Liu, D. J. Xue, J. Y. Ma, J. Ding, H. J. Yan, J. S. Hu and L. J. Wan, *J. Am. Chem. Soc.*, 2016, **138**, 16196–16199.
37 F. Yao, J. L. Peng, R. M. Li, W. J. Li, P. B. Gui, B. R. Li, C. Liu, C. Tao, Q. Q. Lin and G. J. Fang, *Nat. Commun.*, 2020, **11**, 1194.
38 Y. C. Liu, J. K. Sun, Z. Yang, D. Yang, X. D. Ren, H. Xu, Z. P. Yang and S. Z. Liu, *Adv. Opt. Mater.*, 2016, **4**, 1829–1837.
39 Y. B. Mao, S. Banerjee and S. S. Wong, *J. Am. Chem. Soc.*, 2003, **125**, 15718–15719.
40 J. Schlipf, A. M. Askar, F. Pantle, B. D. Wiltshire, A. Sura, P. Schneider, L. Huber, K. Shankar and P. M. Buschbaum, *Sci. Rep.*, 2018, **8**, 4906.
41 S. W. Eaton, A. Fu, A. B. Wong, C. Z. Ning and P. D. Yang, *Nat. Rev. Mater.*, 2016, **1**, 16028.

42 E. Horváth, M. Spina, Z. Szekrényes, K. Kamarás, R. Gaal, D. Gachet and L. Forró, *Nano Lett.*, 2014, **14**, 6761–6766.

43 J. X. Ding, S. J. Du, Z. Y. Zuo, Y. Zhao, H. Z. Cui and X. Y. Zhan, *J. Phys. Chem. C*, 2017, **121**, 4917–4923.

44 J. H. Cha, J. H. Han, W. P. Yin, C. Park, Y. M. Park, T. K. Ahn, J. H. Cho and D. Y. Jung, *J. Phys. Chem. Lett.*, 2017, **8**, 565–570.

45 I. M. Asuo, P. Fourmont, I. Ka, D. Gedamu, S. Bouzidi, A. Pignolet, R. Nechache and S. G. Cloutier, *Small*, 2019, **15**, 1804150.

46 Y. C. Liu, Y. X. Zhang, Z. Yang, J. S. Feng, Z. Xu, Q. X. Li, M. X. Hu, H. C. Ye, X. Zhang, M. Liu, K. Zhao and S. Z. Liu, *Mater. Today*, 2019, **22**, 67–75.

47 Q. R. Lv, Z. P. Lian, W. H. He, J. L. Sun, Q. Li and Q. F. Yan, *J. Mater. Chem. C*, 2018, **6**, 4464–4470.

48 Y. C. Liu, Y. X. Zhang, Z. Yang, D. Yang, X. D. Ren, L. Q. Pang and S. Z. Liu, *Adv. Mater.*, 2016, **28**, 9204–9209.

49 J. J. Zhao, G. L. Kong, S. L. Chen, Q. Li, B. Y. Huang, Z. H. Liu, X. Y. San, Y. J. Wang, C. Wang, Y. C. Zhen, H. D. Wen, P. Gao and J. Y. Li, *Sci. Bull.*, 2017, **62**, 1173–1176.

50 Y. P. Fu, H. M. Zhu, J. Chen, M. P. Hautzinger, X. Y. Zhu and S. Jin, *Nat. Rev. Mater.*, 2019, **4**, 169–188.

51 T. Ye, W. F. Fu, J. K. Wu, Z. K. Yu, X. Y. Jin, H. Z. Chen and H. Y. Li, *J. Mater. Chem. A*, 2016, **4**, 1214–1217.

52 Y. Huang, Y. Zhang, J. L. Sun, X. G. Wang, J. L. Sun, Q. Chen, C. F. Pan and H. P. Zhou, *Adv. Mater. Interfaces*, 2018, **5**, 1800224.

53 Y. Qin, H. J. Zhong, J. J. Intemann, S. F. Leng, M. H. Cui, C. C. Qin, M. Xiong, F. Liu, A. K. Y. Jen and K. Yao, *Adv. Energy Mater.*, 2020, **10**, 1904050.

54 Y. C. Liu, Y. X. Zhang, K. Zhao, Z. Yang, J. S. Feng, X. Zhang, K. Wang, L. Meng, H. C. Ye, M. Liu and S. Z. Liu, *Adv. Mater.*, 2018, **30**, 1707314.

55 V. M. Goldschmidt, *Naturwissenschaften*, 1926, **14**, 477–485.

56 H. P. Rooksby, *Nature*, 1945, **155**, 484.

57 N. K. Kumawat, A. Dey, K. L. Narasimhan and D. Kabra, *ACS Photonics*, 2015, **2**, 349–354.

58 R. Z. Zhuang, X. J. Wang, W. B. Ma, Y. H. Wu, X. Chen, L. H. Tang, H. M. Zhu, J. Y. Liu, L. L. Wu, W. Zhou, X. Liu and Y. Yang, *Nat. Photonics*, 2019, **13**, 602–609.

59 Y. Y. Li, G. L. Zheng, C. K. Lin and J. Lin, *Solid State Sci.*, 2007, **9**, 855–861.

60 W. Y. Zhang, Y. Y. Tang, P. F. Li, P. P. Shi, W. Q. Liao, D. W. Fu, H. Y. Ye, Y. Zhang and R. G. Xiong, *J. Am. Chem. Soc.*, 2017, **139**, 10897–10902.

61 Y. N. Chen, M. H. He, J. J. Peng, Y. Sun and Z. Q. Liang, *Adv. Sci.*, 2016, **3**, 1500392.

62 M. Grätzel, *Nat. Mater.*, 2014, **13**, 838–842.

63 M. A. Green, A. Ho-Baillie and H. J. Snaith, *Nat. Photonics*, 2014, **8**, 506–514.

64 C. H. Li, K. C. K. Soh and P. Wu, *J. Alloy. Compd.*, 2004, **372**, 40–48.

65 Q. D. Sun and W. J. Yin, *J. Am. Chem. Soc.*, 2017, **139**, 14905–14908.

66 D. Weber, *Z. Naturforsch. B*, 1978, **33**, 1443–1445.

67 D. B. Mitzi, *J. Chem. Soc., Dalton Trans.*, 2001, 1–12.

68 N. O. Yamamuro, T. Matsuo and H. Suga, *J. Phys. Chem. Solids*, 1990, **51**, 1383–1395.

69 H. L. Yue, H. H. Sung and F. C. Chen, *Adv. Electron. Mater.*, 2018, **4**, 1700655.

70 X. Li, M. I. Dar, C. Y. Yi, J. S. Luo, M. Tschumi, S. M. Zakeeruddin, M. K. Nazeeruddin, H. W. Han and M. Grätzel, *Nat. Chem.*, 2015, **7**, 703–711.

71 L. N. Quan, M. J. Yuan, R. Comin, O. Voznyy, E. M. Beauregard, S. Hoogland, A. Buin, A. R. Kirmani, K. Zhao, A. Amassian, D. H. Kim and E. H. Sargent, *J. Am. Chem. Soc.*, 2016, **138**, 2649–2655.

72 S. Bai, P. M. Da, C. Li, Z. P. Wang, Z. C. Yuan, F. Fu, M. Kawecki, X. J. Liu, N. Sakai, J. T. W. Wang, S. Huettner, S. Buecheler, M. Fahlman, F. Gao and H. J. Snaith, *Nature*, 2019, **571**, 245–250.

73 I. C. Smith, E. T. Hoke, D. S. Ibarra, M. D. McGehee and H. I. Karunadasa, *Angew. Chem., Int. Ed.*, 2014, **53**, 11232–11235.

74 R. Wang, M. Mujahid, Y. Duan, Z. K. Wang, J. J. Xue and Y. Yang, *Adv. Funct. Mater.*, 2019, **29**, 1808843.

75 Y. L. Song, W. H. Bi, A. Wang, X. T. Liu, Y. F. Kang and Q. F. Dong, *Nat. Commun.*, 2020, **11**, 274.

76 Y. Y. Dang, Y. Liu, Y. X. Sun, D. S. Yuan, X. L. Liu, W. Q. Lu, G. F. Liu, H. B. Xia and X. T. Tao, *CrystEngComm*, 2015, **17**, 665–670.

77 Q. F. Dong, J. F. Song, Y. J. Fang, Y. C. Shao, S. Ducharme and J. S. Huang, *Adv. Mater.*, 2016, **28**, 2816–2821.

78 Q. Wang, B. Chen, Y. Liu, Y. H. Deng, Y. Bai, Q. F. Dong and J. S. Huang, *Energy Environ. Sci.*, 2017, **10**, 516–522.

79 Q. F. Han, S. H. Bae, P. Y. Sun, Y. T. Hsieh, Y. M. Yang, Y. S. Rim, H. X. Zhao, Q. Chen, W. Z. Shi, G. Li and Y. Yang, *Adv. Mater.*, 2016, **28**, 2253–2258.

80 L. Chen, Y. Y. Tan, Z. X. Chen, T. Wang, S. Hu, Z. A. Nan, L. Q. Xie, Y. Hui, J. X. Huang, C. Zhan, S. H. Wang, J. Z. Zhou, J. W. Yan, B. W. Mao and Z. Q. Tian, *J. Am. Chem. Soc.*, 2019, **141**, 1665–1671.

81 M. I. Saidaminov, A. L. Abdelhady, B. Murali, E. Alarousu, V. M. Burlakov, W. Peng, I. Dursun, L. F. Wang, Y. He, G. Maculan, A. Goriely, T. Wu, O. F. Mohammed and O. M. Bakr, *Nat. Commun.*, 2015, **6**, 7586.

82 W. Peng, L. F. Wang, M. Banavoth, K. T. Ho, A. Bera, N. C. Cho, C. F. Kang, V. M. Burlakov, J. Pan, L. Sinatra, C. Ma, W. Xu, D. Shi, E. Alarousu, A. Goriely, J. H. He, O. F. Mohammed, T. Wu and O. Bakr, *Adv. Mater.*, 2016, **28**, 3383–3390.

83 E. M. Hutter, M. C. G. Rueda, A. Osherov, V. Bulović, F. C. Grozema, S. D. Stranks and T. J. Savenije, *Nat. Mater.*, 2017, **16**, 115–120.

84 Z. L. Chen, Q. F. Dong, Y. Liu, C. X. Bao, Y. J. Fang, Y. Lin, S. Tang, Q. Wang, X. Xiao, Y. Bai, Y. H. Deng and J. S. Huang, *Nat. Commun.*, 2017, **8**, 1890.

85 W. Peng, J. Yin, K. T. Ho, O. Ouellette, M. D. Bastiani, B. Murali, O. E. Tall, C. Shen, X. H. Miao, J. Pan, E. Alarousu, J. H. He, B. S. Ooi, O. F. Mohammed, E. Sargent and O. M. Bakr, *Nano Lett.*, 2017, **17**, 4759–4767.

86 D. Shi, V. Adinolfi, R. Comin, M. J. Yuan, E. Alarousu, A. Buin, Y. Chen, S. Hoogland, A. Rothenberger,

K. Katsiev, Y. Losovyj, X. Zhang, P. A. Dowben, O. F. Mohammed, E. H. Sargent and O. M. Bakr, *Science*, 2015, **347**, 519–522.

87 Z. Cheng, K. W. Liu, J. L. Yang, X. Chen, X. H. Xie, B. H. Li, Z. Z. Zhang, L. Liu, C. X. Shan and D. Z. Shen, *ACS Appl. Mater. Inter.*, 2019, **11**, 34144–34150.

88 H. Diab, C. Arnold, F. Lédée, G. T. Allard, G. Delport, C. Vilar, F. Bretenaker, J. Barjon, J. S. Lauret, E. Deleporte and D. Garrot, *J. Phys. Chem. Lett.*, 2017, **8**, 2977–2983.

89 N. J. Jeon, H. Na, E. H. Jung, T. Y. Yang, Y. G. Lee, G. Kim, H. W. Shin, S. Seok, J. Lee and J. Seo, *Nat. Energy*, 2018, **3**, 682–689.

90 M. Pratheek and P. Predeep, *Mater. Chem. Phys.*, 2020, **239**, 122084.

91 Q. F. Dong, Y. J. Fang, Y. C. Shao, P. Mulligan, J. Qiu, L. Cao and J. S. Huang, *Science*, 2015, **347**, 967–970.

92 Y. C. Liu, X. D. Ren, J. Zhang, Z. Yang, D. Yang, F. Y. Yu, J. K. Sun, C. M. Zhao, Z. Yao, B. Wang, Q. B. Wei, F. W. Xiao, H. B. Fan, H. Deng, L. P. Deng and S. Z. Liu, *Sci. China: Chem.*, 2017, **60**, 1367–1370.

93 Y. Yang, Y. Yan, M. J. Yang, S. Choi, K. Zhu, J. M. Luther and M. C. Beard, *Nat. Commun.*, 2015, **6**, 7961.

94 S. D. Stranks, G. E. Eperon, G. Grancini, C. Menelaou, M. J. P. Alcocer, T. Leijtens, L. M. Herz, A. Petrozza and H. J. Snaith, *Science*, 2013, **342**, 341–344.

95 M. I. Saidaminov, V. Adinolfi, R. Comin, A. L. Abdelhady, W. Peng, I. Dursun, M. J. Yuan, S. Hoogland, E. H. Sargent and O. M. Bakr, *Nat. Commun.*, 2015, **6**, 8724.

96 F. Y. Zhang, B. Yang, Y. J. Li, W. Q. Deng and R. X. He, *J. Mater. Chem. C*, 2017, **5**, 8431–8435.

97 L. Wang, G. D. Yuan, R. F. Duan, F. Huang, T. B. Wei, Z. Q. Liu, J. X. Wang and J. M. Li, *AIP Adv.*, 2016, **6**, 045115.

98 M. I. Saidaminov, M. A. Haque, M. Savoie, A. L. Abdelhady, N. Cho, I. Dursun, U. Buttner, E. Alarousu, T. Wu and O. M. Bakr, *Adv. Mater.*, 2016, **28**, 8144–8149.

99 Z. P. Lian, Q. F. Yan, T. T. Gao, J. Ding, Q. R. Lv, C. G. Ning, Q. Li and J. L. Sun, *J. Am. Chem. Soc.*, 2016, **138**, 9409–9412.

100 Y. J. Fang, Q. F. Dong, Y. C. Shao, Y. B. Yuan and J. S. Huang, *Nat. Photonics*, 2015, **9**, 679–686.

101 Y. X. Zhang, Y. C. Liu, Y. Y. Li, Z. Yang and S. Z. Liu, *J. Mater. Chem. C*, 2016, **4**, 9172–9178.

102 F. Y. Zhang, B. Yang, X. Mao, R. X. Yang, L. Jiang, Y. J. Li, J. Xiong, Y. Yang, R. X. He, W. Q. Deng and K. Han, *ACS Appl. Mater. Interfaces*, 2017, **9**, 14827–14832.

103 Y. C. Liu, Z. Yang, D. Cui, X. D. Ren, J. K. Sun, X. J. Liu, J. R. Zhang, Q. B. Wei, H. B. Fan, F. Y. Yu, X. Zhang, C. M. Zhao and S. Z. Liu, *Adv. Mater.*, 2015, **27**, 5176–5183.

104 M. I. Saidaminov, A. L. Abdelhady, G. Maculan and O. M. Bakr, *Chem. Commun.*, 2015, **51**, 17658–17661.

105 Y. Huang, L. Li, Z. H. Liu, H. Y. Jiao, Y. Q. He, X. G. Wang, R. Zhu, D. Wang, J. L. Sun, Q. Chen and H. P. Zhou, *J. Mater. Chem. A*, 2017, **5**, 8537–8544.

106 L. Ma, J. Dai and X. C. Zeng, *Adv. Energy Mater.*, 2017, **7**, 1601731.

107 R. Wang, J. J. Xue, K. L. Wang, Z. K. Wang, Y. Q. Luo, D. Fenning, G. W. Xu, S. Nuryyeva, T. Y. Huang, Y. P. Zhao, J. L. Yang, J. H. Zhu, M. H. Wang, S. Tan, I. Yavuz, K. N. Houk and Y. Yang, *Science*, 2019, **366**, 1509.

108 T. P. Zhao, R. Q. He, T. H. Liu, Y. H. Li, D. Yu, Y. X. Gao, G. Y. Qu, N. Li, C. M. Wang, H. Huang, J. Zhou, S. Bai, S. M. Xiao, Z. L. Chen, Y. M. Chen and Q. H. Song, *ACS Nano*, 2025, **19**, 3282–3292.

109 Z. Y. Ni, C. X. Bao, Y. Liu, Q. Jiang, W. Q. Wu, S. S. Chen, X. Z. Dai, B. Chen, B. Hartweg, Z. S. Yu, Z. Holman and J. S. Huang, *Science*, 2020, **367**, 1352.

110 A. Y. Alsalloum, B. Turedi, X. P. Zheng, S. Mitra, A. A. Zhumekenov, K. J. Lee, P. Maity, I. Gereige, A. AlSaggaf, I. S. Roqan, O. F. Mohammed and O. M. Bakr, *ACS Energy Lett.*, 2020, **5**, 657–662.

111 C. Li, S. Tscheuschner, F. Paulus, P. E. Hopkinson, J. Kießling, A. Köhler, Y. Vaynzof and S. Huettner, *Adv. Mater.*, 2016, **28**, 2446.

112 C. Li, A. Guerrero, S. Huettner and J. Bisquert, *Nat. Commun.*, 2018, **9**, 5113.

113 C. Li, A. Guerrero, Y. Zhong and S. Huettner, *J. Phys. Condens. Matter*, 2017, **29**, 193001.

114 M. H. Futscher, J. M. Lee, L. McGovern, L. A. Muscarella, T. Y. Wang, M. I. Haider, A. Fakharuddin, L. S. Mende and B. Ehrler, *Mater. Horiz.*, 2019, **6**, 1497.

115 Z. G. Xiao, Y. B. Yuan, Y. C. Shao, Q. Wang, Q. F. Dong, C. Bi, P. Sharma, A. Gruverman and J. S. Huang, *Nat. Mater.*, 2015, **14**, 193.

116 J. Xing, Q. Wang, Q. F. Dong, Y. B. Yuan, Y. J. Fang and J. S. Huang, *Phys. Chem. Chem. Phys.*, 2016, **18**, 30484–30490.

117 A. M. A. Leguy, Y. H. Hu, M. C. Quiles, M. I. Alonso, O. J. Weber, P. Azarhoosh, M. V. Schilfgaarde, M. T. Weller, T. Bein, J. Nelson, P. Docampo and P. R. F. Barnes, *Chem. Mater.*, 2015, **27**, 3397–3407.

118 A. Poglitsch and D. Weber, *J. Chem. Phys.*, 1987, **87**, 6373–6378.

119 Z. P. Lian, Q. F. Yan, Q. R. Lv, Y. Wang, L. L. Liu, L. J. Zhang, S. L. Pan, Q. Li, L. D. Wang and J. L. Sun, *Sci. Rep.*, 2015, **5**, 16563.

120 Y. Y. Dang, Y. Zhou, X. L. Liu, D. X. Ju, S. Q. Xia, H. B. Xia and X. T. Tao, *Angew. Chem., Int. Ed.*, 2016, **55**, 3447–3450.

121 F. Y. Yu, Q. J. Han, L. Wang, S. Z. Yang, X. Y. Cai, C. Zhang and T. L. Ma, *Sol. RRL*, 2021, **5**, 2100404.

122 G. Maculan, A. D. Sheikh, A. L. Abdelhady, M. I. Saidaminov, M. A. Haque, B. Murali, E. Alarousu, O. F. Mohammed, T. Wu and O. M. Bakr, *J. Phys. Chem. Lett.*, 2015, **6**, 3781–3786.

123 A. A. Zhumekenov, M. I. Saidaminov, M. A. Haque, E. Alarousu, S. P. Sarmah, B. Murali, I. Dursun, X. H. Miao, A. L. Abdelhady, T. Wu, O. F. Mohammed and O. M. Bakr, *ACS Energy Lett.*, 2016, **1**, 32–37.

124 A. A. Zhumekenov, V. M. Burlakov, M. I. Saidaminov, A. Alofi, M. A. Haque, B. Turedi, B. Davaasuren, I. Dursun, N. Cho, A. M. E. Zohry, M. D. Bastiani, A. Giugni, B. Torre, E. D. Fabrizio, O. F. Mohammed, A. Rothenberger, T. Wu, A. Goriely and O. M. Bakr, *ACS Energy Lett.*, 2017, **2**, 1782–1788.

125 T. Ye, X. Z. Wang, X. Q. Li, A. Q. Yan, S. Ramakrishna and J. W. Xu, *J. Mater. Chem. C*, 2017, **5**, 1255–1260.

126 T. Hattori, T. Taira, M. Era, T. Tsutsui and S. Saito, *Chem. Phys. Lett.*, 1996, **254**, 103.

127 R. Jakubas, G. Bator, M. Gośniowska, Z. Ciunik, J. Baran and J. Lefebvre, *J. Phys. Chem. Solids*, 1997, **58**, 989.

128 W. Q. Liao, Y. Zhang, C. L. Hu, J. G. Mao, H. Y. Ye, P. F. Li, S. P. D. Huang and R. G. Xiong, *Nat. Commun.*, 2015, **6**, 7338.

129 B. Huang, L. Y. Sun, S. S. Wang, J. Y. Zhang, C. M. Ji, J. H. Luo, W. X. Zhang and X. M. Chen, *Chem. Commun.*, 2017, **53**, 5764–5766.

130 M. D. Xiao, F. Z. Huang, W. C. Huang, Y. Dkhissi, Y. Zhu, J. Etheridge, A. G. Weale and U. Bach, *Angew. Chem., Int. Ed.*, 2014, **53**, 9898.

131 N. J. Jeon, J. H. Noh, Y. C. Kim, W. S. Yang, S. Ryu and S. Seok, *Nat. Mater.*, 2014, **13**, 897–903.

132 C. T. Zuo and L. M. Ding, *Angew. Chem., Int. Ed.*, 2017, **56**, 6528–6532.

133 F. Cao, G. Y. Cheng, E. L. Hong, Y. Liu, S. C. Han, P. P. Yu and B. Sun, *J. Mater. Chem. C*, 2025, **13**, 4543–4548.

134 Y. P. Wang, Y. F. Shi, G. Q. Xin, J. Lian and J. Shi, *Cryst. Growth Des.*, 2015, **15**, 4741–4749.

135 Y. L. Wang, X. Guan, D. H. Li, H. C. Cheng, X. D. Duan and Z. Y. Lin, *Nano Res.*, 2017, **10**, 1223–1233.

136 Y. Zhou, K. Fernando, J. Y. Wan, F. Z. Liu, S. Shrestha, J. Tisdale, C. J. Sheehan, A. C. Jones, S. Tretiak, H. Tsai, H. H. Huang and W. Y. Nie, *Adv. Funct. Mater.*, 2021, **31**, 2101058.

137 T. Musálek, P. Liška, A. Morsa, J. A. Arregi, P. Klok, M. Kratochvíl, D. Sergeev, M. Müller, T. Šikola and M. Kolíbal, *APL Mater.*, 2025, **13**, 031118.

138 P. Zhang, Y. Q. Hua, X. Li, L. Z. Zhang, L. Liu, R. Z. Li, G. D. Zhang and X. T. Tao, *J. Mater. Chem. C*, 2021, **9**, 2840–2847.

139 C. C. Stoumpos, C. D. Malliakas, J. A. Peters, Z. F. Liu, M. Sebastian, J. Im, T. C. Chasapis, A. C. Wibowo, D. Y. Chung, A. J. Freeman, B. W. Wessels and M. G. Kanatzidis, *Cryst. Growth Des.*, 2013, **13**, 2722–2727.

140 P. Zhang, G. D. Zhang, L. Liu, D. X. Ju, L. Z. Zhang, K. Cheng and X. T. Tao, *J. Phys. Chem. Lett.*, 2018, **9**, 5040–5046.

141 Y. H. He, C. C. Stoumpos, I. Hadar, Z. Z. Luo, K. M. McCall, Z. F. Liu, D. Y. Chung, B. W. Wessels and M. G. Kanatzidis, *J. Am. Chem. Soc.*, 2021, **143**, 2068–2077.

142 P. A. Shaikh, D. Shi, J. R. D. Retamal, A. D. Sheikh, M. A. Haque, C. F. Kang, J. H. He, O. M. Bakr and T. Wu, *J. Mater. Chem. C*, 2016, **4**, 8304–8312.

143 Z. Q. Yang, Y. H. Deng, X. W. Zhang, S. Wang, H. Z. Chen, S. Yang, J. Khurgin, N. X. Fang, X. Zhang and R. Ma, *Adv. Mater.*, 2018, **30**, 1704333.

144 W. Deng, X. J. Zhang, L. M. Huang, X. Z. Xu, L. Wang, J. C. Wang, Q. X. Shang, S. T. Lee and J. S. Jie, *Adv. Mater.*, 2016, **28**, 2201–2208.

145 J. Wu, F. J. Ye, W. Q. Yang, Z. J. Xu, D. Y. Luo, R. Su, Y. F. Zhang, R. Zhu and Q. H. Gong, *Chem. Mater.*, 2018, **30**, 4590–4596.

146 Q. Liao, K. Hu, H. H. Zhang, X. D. Wang, J. N. Yao and H. B. Fu, *Adv. Mater.*, 2015, **27**, 3405–3410.

147 J. Xing, X. F. Liu, Q. Zhang, S. T. Ha, Y. W. Yuan, C. Shen, T. C. Sum and Q. H. Xiong, *Nano Lett.*, 2015, **15**, 4571–4577.

148 Z. Y. Zhang, K. Yu and G. P. Wang, *Adv. Electron. Mater.*, 2019, **5**, 1900718.

149 J. Ding, H. J. Fang, Z. P. Lian, J. W. Li, Q. R. Lv, L. D. Wang, J. L. Sun and Q. F. Yan, *CrystEngComm*, 2016, **18**, 4405–4411.

150 M. Cao, J. Y. Tian, Z. Cai, L. Peng, L. Yang and D. C. Wei, *Appl. Phys. Lett.*, 2016, **109**, 233303.

151 J. S. Luo, J. X. Xia, H. Yang, L. L. Chen, Z. Q. Wan, F. Han, H. A. Malik, X. H. Zhu and C. Y. Jia, *Energy Environ. Sci.*, 2018, **11**, 2035–2045.

152 Z. L. Chen, B. Turedi, A. Y. Alsalloum, C. Yang, X. P. Zheng, I. Gereige, A. AlSaggaf, O. F. Mohammed and O. M. Bakr, *ACS Energy Lett.*, 2019, **4**, 1258–1259.

153 B. Náfrádi, G. Náfrádi, L. Forró and E. Horváth, *J. Phys. Chem. C*, 2015, **119**, 25204–25208.

154 C. Szeles, *Phys. Status Solidi B*, 2004, **241**, 783–790.

155 S. Yakunin, M. Sytnyk, D. Kriegner, S. Shrestha, M. Richter, G. J. Matt, H. Azimi, C. J. Brabec, J. Stangl, M. V. Kovalenko and W. Heiss, *Nat. Photonics*, 2015, **9**, 444–449.

156 S. D. Sordo, L. Abbene, E. Caroli, A. M. Mancini, A. Zappettini and P. Ubertini, *Sensors*, 2009, **9**, 3491–3526.

157 S. Yakunin, D. N. Dirin, Y. Shynkarenko, V. Morad, I. Cherniukh, O. Nazarenko, D. Kreil, T. Nauser and M. V. Kovalenko, *Nat. Photonics*, 2016, **10**, 585–589.

158 H. T. Wei, D. DeSantis, W. Wei, Y. H. Deng, D. Y. Guo, T. J. Savenije, L. Cao and J. S. Huang, *Nat. Mater.*, 2017, **16**, 826–833.

159 Y. Shen, Y. C. Liu, H. C. Ye, Y. T. Zheng, Q. Wei, Y. D. Xia, Y. H. Chen, K. Zhao, W. Huang and S. Z. Liu, *Angew. Chem., Int. Ed.*, 2020, **59**, 14896–14902.

160 L. Pan, Z. F. Liu, C. Welton, V. V. Klepov, J. A. Peters, M. C. D. Siena, A. Benadia, I. Pandey, A. Miceli, D. Y. Chung, G. N. M. Reddy, B. W. Wessels and M. G. Kanatzidis, *Adv. Mater.*, 2023, **35**, 2211840.

161 N. M. Liu, D. P. Chu, X. Q. Xin, J. Y. Tian, Y. J. Jiang, N. Liang, B. X. Jia, Y. C. Liu and S. Z. Liu, *Adv. Funct. Mater.*, 2025, 2504203.

162 M. D. Birowosuto, D. Cortecchia, W. Drozdowski, K. Brylew, W. Lachmanski, A. Bruno and C. Soci, *Sci. Rep.*, 2016, **6**, 37254.

163 Q. Xu, W. Y. Shao, J. Liu, Z. C. Zhu, X. Ouyang, J. F. Cai, B. Liu, B. Liang, Z. Y. Wu and X. P. Ouyang, *ACS Appl. Mater. Interfaces*, 2019, **11**, 47485–47490.

164 W. Y. Shao, Y. Li, X. Wang, X. Ouyang, J. F. Cai, C. Li, X. P. Ouyang, Z. Y. Wu and Q. Xu, *Phys. Chem. Chem. Phys.*, 2020, **22**, 6970–6974.

165 J. Liu, W. Y. Shao, Q. Xu, Y. Liu and X. P. Ouyang, *IEEE Photonic Tech. Lett*, 2020, **32**, 635–638.

166 A. Xie, T. H. Nguyen, C. Hettiarachchi, M. E. Witkowski, W. Drozdowski, M. D. Birowosuto, H. Wang and C. Dang, *J. Phys. Chem. C*, 2018, **122**, 16265–16273.

167 Z. H. Zhu, W. Li, W. Deng, W. D. He, C. Yan, X. D. Peng, X. K. Zeng, Y. Gao, X. H. Fu, N. Lin, B. Gao and W. Q. Yang, *J. Mater. Chem. C*, 2022, **10**, 6837–6845.

168 B. X. Jia, D. P. Chu, N. Li, Y. X. Zhang, Z. Yang, Y. J. Hu, Z. Q. Zhao, J. S. Feng, X. D. Ren, H. Zhang, G. T. Zhao, H. M. Sun, N. Y. Yuan, J. N. Ding, Y. C. Liu and S. Z. Liu, *ACS Energy Lett.*, 2023, **8**, 590–599.

169 L. Zi, J. Song, N. Wang, T. Y. Wang, W. Li, H. C. Zhu, W. Xu and H. W. Song, *Laser Photonics Rev.*, 2023, **17**, 2200852.

170 L. S. Liu, M. X. Xu, X. G. Xu, X. T. Tao and Z. L. Gao, *Adv. Mater.*, 2024, **36**, 2406443.

171 B. M. Yang, X. Ouyang, X. Zhao, J. Su, Y. Li, S. Y. Zhang and X. P. Ouyang, *InfoMat*, 2025, **7**, e12648.

172 Z. K. Tan, R. S. Moghaddam, M. L. Lai, P. Docampo, R. Higler, F. Deschler, M. Price, A. Sadhanala, L. M. Pazos, D. Credgington, F. Hanusch, T. Bein, H. J. Snaith and R. H. Friend, *Nat. Nanotechnol.*, 2014, **9**, 687–692.

173 Y. H. Kim, H. C. Cho, J. H. Heo, T. S. Kim, N. Myoung, C. L. Lee, S. H. Im and T. W. Lee, *Adv. Mater.*, 2015, **27**, 1248–1254.

174 J. Q. Li, S. G. R. Bade, X. Shan and Z. B. Yu, *Adv. Mater.*, 2015, **27**, 5196–5202.

175 R. L. Z. Hoye, M. R. Chua, K. P. Musselman, G. R. Li, M. L. Lai, Z. K. Tan, N. C. Greenham, J. L. Driscoll, R. H. Friend and D. Credgington, *Adv. Mater.*, 2015, **27**, 1414–1419.

176 A. B. Wong, M. L. Lai, S. W. Eaton, Y. Yu, E. Lin, L. Dou, A. Fu and P. D. Yang, *Nano Lett.*, 2015, **15**, 5519–5524.

177 M. M. Chen, X. Shan, T. Geske, J. Q. Li and Z. B. Yu, *ACS Nano*, 2017, **11**, 6312–6318.

178 Y. C. Ling, Z. Yuan, Y. Tian, X. Wang, J. C. Wang, Y. Xin, K. Hanson, B. W. Ma and H. W. Gao, *Adv. Mater.*, 2016, **28**, 305–311.

179 V. C. Nguyen, H. Katsuki, F. Sasaki and H. Yanagi, *Jpn. J. Appl. Phys.*, 2018, **57**, 04FL10.

180 Z. Gao, Y. F. Zheng, D. Zhao and J. S. Yu, *Nanomaterials*, 2018, **8**, 787.

181 H. Y. Zhang, T. X. Yu, C. Q. Wang, R. F. Jia, A. A. A. Pirzado, D. Wu, X. J. Zhang, X. H. Zhang and J. S. Jie, *ACS Nano*, 2022, **16**, 6394–6403.

182 W. Zhang, Y. F. Wang, H. Y. Xiang, Y. S. Wang, F. Wu, Z. C. Bai, Q. Zhang and Y. Chen, *Mater. Lett.*, 2025, **389**, 138274.

183 J. H. Guo, L. T. Li, B. Liu, Y. Tang, L. Qin, Z. B. Deng, Z. D. Lou, Y. F. Hu, F. Teng and Y. B. Hou, *J. Mater. Chem. C*, 2023, **11**, 3030–3038.

184 P. P. Ma, L. H. Yan, J. H. Si, T. Y. Huo, Z. Q. Huang, W. J. Tan, J. Xu and X. Hou, *Laser Photonics Rev.*, 2023, **17**, 2300533.

185 G. C. Xing, N. Mathews, S. S. Lim, N. Yantara, X. F. Liu, D. Sabba, M. Grätzel, S. Mhaisalkar and T. C. Sum, *Nat. Mater.*, 2014, **13**, 476–480.

186 Q. Zhang, S. T. Ha, X. F. Liu, T. C. Sum and Q. H. Xiong, *Nano Lett.*, 2014, **14**, 5995–6001.

187 Z. S. Xu, X. Han, W. Q. Wu, F. T. Li, R. Wang, H. Lu, Q. C. Lu, B. H. Ge, N. Y. Cheng, X. Y. Li, G. J. Yao, H. Hong, K. H. Liu and C. F. Pan, *Light Sci. Appl.*, 2023, **12**, 67.

188 S. Aoyagi, Z. Su, G. E. Weng, S. J. Ye, F. Y. Cao, C. Wang, X. B. Hu, Y. Yamamoto and S. Q. Chen, *Opt. Lett.*, 2025, **50**, 702–705.

189 M. A. Green, E. D. Dunlop, M. Yoshita, N. Kopidakis, K. Bothe, G. Siefer, X. J. Hao and J. Y. Jiang, *Prog. Photovolt. Res. Appl.*, 2025, **33**, 795–810.

190 M. N. Lintangpradipto, H. W. Zhu, B. Y. Shao, W. J. Mir, L. Gutiérrez-Arzaluz, B. Turedi, M. Abulikemu, O. F. Mohammed and O. M. Bakr, *ACS Energy Lett.*, 2023, **8**, 4915–4922.

191 A. Y. Alsalloum, B. Turedi, K. Almasabi, X. P. Zheng, R. Naphade, S. D. Stranks, O. F. Mohammed and O. M. Bakr, *Energy Environ. Sci.*, 2021, **14**, 2263–2268.

192 H. Chen, C. Liu, J. Xu, A. Maxwell, W. Zhou, Y. Yang, Q. L. Zhou, A. S. R. Bati, H. Y. Wan, Z. W. Wang, L. W. Zeng, J. K. Wang, P. Serles, Y. Liu, S. Teale, Y. J. Liu, M. I. Saidaminov, M. Z. Li, N. Rolston, S. Hoogland, T. Filleter, M. G. Kanatzidis, B. Chen, Z. J. Ning and E. H. Sargent, *Science*, 2024, **384**, 189–193.

193 S. Zhang, F. Y. Ye, X. Y. Wang, R. Chen, H. D. Zhang, L. Q. Zhan, X. Y. Jiang, Y. W. Li, X. Y. Ji, S. J. Liu, M. J. Yu, F. R. Yu, Y. L. Zhang, R. H. Wu, Z. H. Liu, Z. J. Ning, D. Neher, L. Y. Han, Y. Z. Lin, H. Tian, W. Chen, M. Stolterfoht, L. J. Zhang, W. H. Zhu and Y. Z. Wu, *Science*, 2023, **380**, 404–409.

194 F. Ye, T. Tian, J. Su, R. X. Jiang, J. Li, C. K. Jin, J. H. Tong, S. Bai, F. Z. Huang, P. Müller-Buschbaum, Y. B. Cheng and T. L. Bu, *Adv. Energy Mater.*, 2024, **14**, 2302775.

195 K. Ma, H. R. Atapattu, Q. Zhao, Y. Gao, B. P. Finkenauer and K. Wang, *Adv. Mater.*, 2021, **33**, 2100791.

196 T. Wang, Y. Li, Q. Cao, J. Yang, B. Yang, X. Pu and X. Pu, *Energy Environ. Sci.*, 2022, **15**, 4414–4424.

197 S. F. Wu, Z. Li, M. Q. Li, Y. X. Diao, F. Lin, T. T. Liu, J. Zhang, P. Tieu, W. P. Gao, F. Qi, X. Q. Pan, Z. T. Xu, Z. L. Zhu and A. K. Y. Jen, *Nat. Nanotechnol.*, 2020, **15**, 934–940.

198 X. Zhang, D. Zhao, Z. Huo, J. Sun, Y. Hu, Z. Lou, Y. Hou, F. Teng and Q. Cui, *Opt. Mater.*, 2021, **117**, 111074.

199 X. Li, C. Liu, F. Ding, Z. Lu, P. Gao, Z. Huang, W. Dang, L. Zhang, X. Lin, S. Ding, B. Li, Y. Huangfu, X. Shen, B. Li, X. Zou, Y. Liu, L. Liao, Y. Wang and X. Duan, *Adv. Funct. Mater.*, 2023, **33**, 2213360.

200 F. X. Liang, L. L. Zhou, Y. Hu, S. F. Li, Z. Y. Zhang, J. Y. Li, C. Fu, C. Y. Wu, L. Wang, J. A. Huang and L. B. Luo, *Adv. Funct. Mater.*, 2023, **33**, 2302175.

201 M. J. Sun, Z. H. Li, L. Liang, T. Chen, Q. Lou, L. Zhao, J. Z. Wang, X. X. Xu, B. S. Zhang, Y. F. Jin and H. Zhou, *Adv. Mater. Technol.*, 2025, **10**, 70050.

202 T. P. Zhao, R. Q. He, T. H. Liu, Y. H. Li, D. Yu, Y. X. Gao, G. Y. Qu, N. Li, C. M. Wang, H. Huang, J. Zhou, S. Bai, S. M. Xiao, Z. L. Chen, Y. M. Chen and Q. H. Song, *ACS Nano*, 2025, **19**, 3282–3292.

203 S. Zhan, Y. W. Duan, Z. K. Liu, L. Yang, K. He, Y. H. Che, W. J. Zhao, Y. Han, S. M. Yang, G. T. Zhao, N. Y. Yuan Ningyi, J. N. Ding and S. Z. Liu, *Adv. Energy Mater.*, 2022, **12**, 2200867.